

Estimation of the Peak Power Density in the Vicinity of Cellular and Radio Base Station Antennas

Renato Cicchetti ¹, Senior Member IEEE, Antonio Faraone (*) ², Member IEEE

¹ University of Rome "La Sapienza"

Department of Electronics Engineering

Rome, Italy

² (*) Corresponding author

Motorola Labs - Corporate EME Research Laboratory

8000 West Sunrise Blvd, Fort Lauderdale, FL 33322, USA

Phone: +1-954-723-4413; Fax: +1-954-723-5611

Email: antonio.faraone@motorola.com

ABSTRACT

Prediction formulae for estimating the peak equivalent power density in the near-field of cellular basestation array antennas are demonstrated. Theoretical justification stemming from a uniform asymptotic expansion of the field radiated by collinear arrays is described, and verification is carried out by means of an extensive computational analysis of different classes of base station antennas. The formulae, which depend on a few, readily available parameters, can be conveniently employed for the estimation of compliance distances with respect to RF safety guidelines issued by the International Committee on Non-Ionizing Radiation Protection (ICNIRP), which have been adopted in many countries throughout the world, without requiring extensive and expensive near-field measurements campaigns.

Submitted: March 10, 2003. Revised: August 14, 2003.

I. INTRODUCTION

The most widely adopted international RF safety guidelines are those issued by the IEEE [1] and by the International Commission on Non-Ionizing Radiation Protection (ICNIRP) [2]. They both establish free-space incident field limits for the human exposure to RF energy sources. However, in both cases the primary dosimetric quantity for assessing the human exposure to electromagnetic fields is the *specific absorption rate* (SAR), i.e., the time-rate of RF energy absorption per unit mass [3]. Correspondingly, the techniques enabling compliance assessments belong to the fields of *RF densitometry* or *RF dosimetry*.

The IEEE C95.1-1999 Standard establishes so called *maximum permissible exposure* (MPE) limits for free-space field quantities such as the *rms* electric and magnetic fields, and the corresponding equivalent power density. The rationale is that meeting MPE limits ensures SAR compliance as well, thus enabling the choice of simpler densitometry techniques rather than far more complex SAR measurements [4] for compliance assessments. The ICNIRP guidelines follow essentially the same approach by defining "reference limits" for the free-space incident field quantities. Both documents also differentiate between *controlled* and *uncontrolled environment* [1] (called *occupational* and *general population* exposure in [2]) by introducing a five-fold limit reduction for the latter. Exposure levels experienced in the near-field of basestation arrays are typically in the range of the occupational limits, and the corresponding compliance distances may restrict the activity of personnel engaged in maintenance or installation activities on towers or rooftops. The IEEE MPE limits have been adopted by the FCC (Federal Communications Commission) in the United States, as well as by regulatory agencies in several other countries. Many other countries, including most of Western Europe, have adopted the ICNIRP guidelines as the basis for their respective RF exposure standards.

Besides minor differences in exposure thresholds, the IEEE and ICNIRP guidelines differ

in the way the exposure level is assessed: *average* over the bystander's projection area (in practice, the height) for IEEE, *point-peak* for ICNIRP. In the far-field of large radiators such as base station antennas, the peak and average incident field are about the same, so the mentioned distinction is not likely to make a significant difference when assessing compliance for the general population. However, the near-field distribution along a line parallel to the array axis can be highly irregular because it is produced by superposition of the field radiated by each array element. Therefore, the average and the peak equivalent power density are different in the Fresnel region of the array, before the onset of the far-field propagation regime.

RF exposure compliance at and near radio base station installations

Many researchers have addressed the problem of providing convenient and accurate methods for assessing RF exposure compliance in the proximity of base station installations. MPE measurements and simulation techniques are recommended in [5]-[6]. In [7], a practical method to carry out broadband and narrowband on-site surveys is discussed. A methodology based on near-field measurements is presented in [8]. MPE can also be determined analytically by summing-up the radiated field by individual array element, as described in [9]-[11]. Ray-tracing techniques, which allow to model accurately urban and suburban environments, have been employed in [12]-[13]. Methodologies to estimate SAR have been developed as well. The use of a massively parallel computational approach based on the application of the Finite-Difference Time-Domain (FDTD) method to very large computational domains is reported in [14]. Hybrid methods are frequently preferred, to limit the FDTD domain to the volumes immediately surrounding the antenna and the exposed subject. A clever combination of measurements and FDTD simulation is proposed in [15]-[16], yielding a methodology that can be applied at any distance from the base station antenna. Similarly, the hybrid computational technique described in [17] can be applied

in the near and far-field regions. Finally, the hybrid computational techniques described in [18]-[19] can be usefully employed to estimate SAR in exposed subjects in the antenna far-field, taking urban environment into account. Recently, many of the above mentioned techniques were summarized and employed to devise a compliance assessment methodology in [20].

Recently, we have studied the propagation characteristics of the electromagnetic field radiated by collinear array antennas employed in base station installations [21]-[22]. The antenna near-field was shown to exhibit a marked cylindrical character up to large electrical distance from the array, for both omnidirectional and sector arrays. This analysis provided theoretical justification to the observations reported in [23], [24], based on measurements at broadside of a collinear array, which led to the introduction of the cylindrical prediction model into compliance guidelines [5]-[6]. In [21], a set of simple formulae was derived to enable the estimation of the *average* equivalent power density in the array near-field, thus yielding a simple method for establishing compliance distances according to the IEEE safety standard. Prediction formulae for reflector-backed arrays were derived as well, supported by experimental validation. However, the formulae proposed in [21] would not enable compliance assessments per the ICNIRP guidelines, which require the estimation of the *peak* value of the power density. The present paper attempts to fill this gap by addressing the estimation of the *peak* incident power density, which is the relevant compliance parameter in all those countries that have adopted the ICNIRP guidelines. In particular, we will establish an upper bound for the peak-to-average power density ratio along the broadside direction, i.e., where the highest exposure occurs. Based on the spatial-average power density definition in [21], and adopting the reference frame in Fig. 1, said ratio is defined as

$$R_{peak} = \max_{\rho \geq \lambda} \left\{ \frac{\max_{|z| < L/2} [S_\rho(\rho, z)]}{\text{avg}_{|z| < L/2} [S_\rho(\rho, z)]} \right\} = \frac{\hat{S}_\rho(\rho_{peak})}{\bar{S}_\rho(\rho_{peak})}, \quad (1)$$

where ρ_{peak} is the radial distance where the peak ratio occurs, while the local equivalent power flow density along a generic radial direction $\hat{\mathbf{r}}$ is defined as

$$S_r(\mathbf{r}) = \lim_{T \rightarrow \infty} \frac{1}{T} \int_0^T \mathbf{E}(\mathbf{r}; \tau) \times \mathbf{H}(\mathbf{r}; \tau) \cdot \hat{\mathbf{r}} d\tau = \text{Re} \left\{ \frac{1}{2} \mathbf{E}(\mathbf{r}) \times \mathbf{H}^*(\mathbf{r}) \cdot \hat{\mathbf{r}} \right\}. \quad (2)$$

where the last equality holds for harmonic signals, assuming (and suppressing) from here on a time dependence $e^{j\omega t}$. The peak-to-average power density ratio (1) will be suitably incorporated in the *average* power density formulae established in [21] to yield prediction formulae for the *peak* power density. Notice that the equivalent power density (2) differs from the one computed based on the E-field or H-field magnitudes [1]. As discussed in [21], such a difference is particularly significant in the reactive near-field of the array elements, which is why the validity range of our analysis is stated for distances greater than one wavelength, while SAR measurements are required at shorter distance.

The paper is structured as follows. In Section II, a uniform asymptotic expansion of the array near-field is outlined, which allows establishing the main characteristics of the peak power density in the Fresnel region of the array field. In Section III, upon correlating peak and average power density, a set of simple formulae for the estimation of the peak power density in the array near-field is derived for both omnidirectional and sector arrays, and their validity range is discussed. Simplified prediction formulae for the compliance distance are also proposed in Section III. The results of the extensive validation performed on the formulae are reported in Section IV, and concluding remarks are presented in Section V.

II. ASYMPTOTIC FIELD EXPANSION NEAR COLLINEAR ARRAYS

For a better understanding of the topic presented in this section, a synthetic description of the asymptotic methodology developed in [22] to analyze the field radiated from arbitrary collinear array antennas is provided in Appendix A. The reader is encouraged to consult [22] for a thorough examination of the subject.

A collinear array antenna is sketched in Fig. 1. The array of length L is formed by collinear wire radiators placed along the z -axis of a cylindrical reference system $(\hat{\rho}, \hat{\phi}, \hat{z})$. Our goal is to establish the physical law governing the spatial evolution of the power density produced by collinear array antennas that radiate broadside, such as those employed in cellular and radio base stations. Therefore, without loss of generality, we focus our attention on the spatial distribution of the fundamental (zero-th order) *Truncated Progressive Floquet Wave (TPFW)*, which features the highest relative strength broadside [22]. In particular, we will analyze the field behavior on the $z = 0$ plane, because that is where the phase combination of the diffracted and *geometrical optics (GO)* fields produces the widest magnitude swings of the fundamental *TPFW* total field, as it will be clear from the corresponding electromagnetic field expressions. Within the limitations discussed in next Section, the ensuing formulation is applicable to broadside arrays that exhibit slight electrical down-tilt of the radiation pattern.

The electromagnetic field components that contribute to real power flow along the radial direction ρ on the $z = 0$ plane are

$$E_z(\rho, 0) \sim -j\omega\mu_0 \frac{I_0}{4\pi} \sqrt{\frac{2\pi}{\beta\rho}} e^{-j\left(\beta\rho + \frac{\pi}{4}\right)} \cdot \left\{ 1 - \sqrt{\frac{\beta\rho}{2\pi}} \frac{4}{\beta L} \left(\frac{\rho}{r}\right)^2 \left[1 + \left(\frac{r}{\rho}\right)^2 \sqrt{\frac{1}{2}\left(1 + \frac{r}{\rho}\right)} (F_i[j\beta(r-\rho)] - 1) \right] e^{-j\left[\beta(r-\rho) + \frac{\pi}{4}\right]} \right\} \quad (3)$$

$$H_\phi(\rho, 0) \sim j\beta \frac{I_0}{4\pi} \sqrt{\frac{2\pi}{\beta\rho}} e^{-j\left(\beta\rho + \frac{\pi}{4}\right)} \cdot \left\{ 1 - \sqrt{\frac{\beta\rho}{2\pi}} \frac{4}{\beta L} \left(\frac{\rho}{r}\right) \left[1 + \left(\frac{r}{\rho}\right) \sqrt{\frac{1}{2} \left(1 + \frac{r}{\rho}\right)} \left(F_t[j\beta(r-\rho)] - 1 \right) \right] e^{-j\left[\beta(r-\rho) + \frac{\pi}{4}\right]} \right\} \quad (4)$$

where β and μ_0 are the free-space wavenumber and magnetic permeability, ω is the angular frequency, while

$$r = \sqrt{\rho^2 + (L/2)^2} \quad (5)$$

is the distance from the array tips, and $F_t(\cdot)$ is the transition function defined in Appendix B.

Using the large argument asymptotic representation of the transition function $F_t(\cdot)$ as $\rho \rightarrow 0$, it is possible to express the field components E_z and H_ϕ along broadside ($z = 0$), before the transition toward the spherical wave-propagation regime, as follows

$$E_z(\rho, 0) \sim -j\omega\mu_0 \frac{I_0}{4\pi} \sqrt{\frac{2\pi}{\beta\rho}} e^{-j\left(\beta\rho + \frac{\pi}{4}\right)} \left\{ 1 - \sqrt{\frac{\beta\rho}{2\pi}} \left(\frac{\rho}{r}\right)^2 \frac{4}{\beta L} e^{-j\left[\beta(r-\rho) + \frac{\pi}{4}\right]} \right\}, \quad (6)$$

$$H_\phi(\rho, 0) \sim j\beta \frac{I_0}{4\pi} \sqrt{\frac{2\pi}{\beta\rho}} e^{-j\left(\beta\rho + \frac{\pi}{4}\right)} \left\{ 1 - \sqrt{\frac{\beta\rho}{2\pi}} \left(\frac{\rho}{r}\right) \frac{4}{\beta L} e^{-j\left[\beta(r-\rho) + \frac{\pi}{4}\right]} \right\}, \quad (7)$$

These expressions clearly show that the typical cylindrical wave character of the *GO* field dominates near the antenna axis. The terms in braces express the field perturbation caused by diffraction at the array truncations.

The *rms* equivalent power density along broadside ($\rho > \lambda_0$) is computed as follows

$$S_\rho(\rho, 0) \simeq -\frac{1}{2} \text{Re} \{ E_z(\rho, 0) H_\phi^*(\rho, 0) \} (\hat{z} \times \hat{\phi}) \cdot \hat{\rho} = S_{cyl}^{GO}(\rho) \text{Re} \{ T(\rho, 0) \}, \quad (8)$$

where $S_{cyl}^{GO}(\rho) = W_{rad}/2\pi\rho L$ is the *GO*-field equivalent power density (derived in Appendix C),

and

$$T(\rho, 0) = 1 + \frac{\beta \rho}{2\pi} \left(\frac{\rho}{r}\right)^3 \left(\frac{4}{\beta L}\right)^2 - \sqrt{\frac{\beta \rho}{2\pi}} \left(\frac{\rho}{r}\right) \frac{4}{\beta L} \left\{ e^{j\left[\beta(r-\rho) + \frac{\pi}{4}\right]} + \left(\frac{\rho}{r}\right) e^{-j\left[\beta(r-\rho) + \frac{\pi}{4}\right]} \right\}. \quad (9)$$

Interference processes, which are modulated by the phase difference between the *GO* and the diffracted field contributions, produce the oscillating term $\text{Re}\{T(\rho, 0)\}$. As shown in Appendix D, this term peaks at a distance

$$\rho_{peak} \simeq \frac{2}{5} \frac{L^2}{\lambda_0}, \quad (10)$$

where the array field begins to decay towards the spherical wave-propagation regime. The corresponding peak overshoot $\text{Re}\{T(\rho_{peak}, 0)\}$ of the local equivalent power density with respect to its average value S_{cyl}^{GO} features the following limit value for very large arrays ($\beta L \rightarrow \infty$)

$$R_{peak} \simeq \text{Re}\{T(\rho_{peak}, 0)\} \rightarrow 1 + 4 \frac{2 + \sqrt{10}\pi \cos \frac{\pi}{8}}{5\pi^2} = 1.906 \approx 2. \quad (11)$$

The fluctuation of the term $\text{Re}\{T(\rho, 0)\}$ with the distance is displayed in Fig. 2 for different electrical length L/λ_0 of the antenna, showing the accuracy of (10) in predicting ρ_{peak} (the vertical dotted line indicates the equation's domain of validity). The accuracy of (11) can be inferred from Fig. 2 as well, which shows the monotonic increase of R_{peak} versus the array's length. Notice that the limit (11) is substantially reached for $L/\lambda_0 \geq 4$, i.e., for the vast majority of antennas used in cellular basestation installations. By using $R_{peak} \approx 2$ for shorter arrays ($L/\lambda_0 < 4$), for instance those employed in many VHF or UHF dispatch systems, a conservative bias is introduced in the assessment.

As a final observation, notice that Eq. (9) can be written as a function of only two pa-

rameters, i.e., the array electrical length (L / λ_0) and the electrical distance from it (ρ / λ_0).

III. PREDICTION FORMULAE FOR THE SPATIAL-PEAK POWER DENSITY

We addressed the problem of deriving simplified expressions for the spatial-average power density due to array antennas in [21]. Spatial averaging is intended along a line parallel to the array axis, having the same length as the array. The ensuing prediction formulae enable the assessment of the *RF* exposure compliance in many practical situations. However, there are other cases where they are not useful because the applicable regulations require estimating the *peak* power density [2], *not* the average, at some distance from the antenna. The results presented in the previous section lead to a straightforward solution of this problem.

Let us start from the *average* power density prediction formula proposed in [21] for omnidirectional collinear arrays, that we herewith rewrite in terms of the *GO*-field equivalent power density

$$\bar{S}_\rho(\rho) = \frac{S_{cyl}^{GO}(\rho)}{\sqrt{1 + \left(\frac{\rho}{\rho_0}\right)^2}}, \quad \rho_0 = D_A \frac{L}{2}, \quad (12)$$

where D_A is the antenna broadside directivity. This formula does not account for the field fluctuations caused by the diffraction phenomena due to the array truncation. As a consequence, it underestimates significantly the peak power density in the neighborhood of ρ_{peak} . However, since we were able to establish an upper bound for the peak-to-average power density ratio ($R_{peak} \simeq 2$), it is possible to modify (12) to produce an estimate for the peak power density. Upon introducing the magnifying factor $R_{peak} \simeq 2$ in (12) to account for the peak-to-average power density ratio in the array near-field, the peak power density produced by omnidirectional collin-

ear arrays can be predicted as follows

$$\hat{S}_\rho(\rho) = \frac{S_{cyl}^{GO}(\rho) R_{peak}}{\sqrt{1 + \left(R_{peak} \frac{\rho}{\rho_0}\right)^2}} \simeq \frac{W_{rad}}{\pi \rho L \sqrt{1 + \left(2 \frac{\rho}{\rho_0}\right)^2}}, \quad \rho_0 = D_A \frac{L}{2}, \quad (13)$$

where W_{rad} is the net radiated power, which can be expressed as $W_{rad} = e_A \cdot W_{fwd}$, where e_A is the antenna efficiency accounting for ohmic and mismatch losses, and W_{fwd} is the forward power at the antenna connector, where conducted power measurements can be performed. This formula allows the accurate estimation of the equivalent power density at the distance ρ_{peak} while providing an overestimate at closer distances, thus enabling conservative compliance assessments near basestation installations. Notice that the factor R_{peak} appears also at the denominator in (13) so as to yield the conventional expression of the power density in the far-field region

$$\hat{S}_\rho(\rho) = \bar{S}_\rho(\rho) = S_{cyl}^{GO}(\rho) \frac{D_A L}{2\rho} = \frac{D_A W_{rad}}{4\pi\rho^2} \quad . \quad (14)$$

The formula for omnidirectional arrays can be modified for sector arrays by taking into account their azimuth pattern $\Phi(\phi)$, as outlined in Appendix E. In this paper, we follow a slightly different approach compared to [21] to derive the sector-array formula, which is preferable as it does not require knowledge of the back-reflector's angle, whereby the peak power density prediction formula for sector arrays becomes

$$\hat{S}_\rho(\rho, \phi) \simeq \frac{W_{rad} 2^{-(\phi/\bar{\phi}_{3dB})^2}}{\bar{\phi}_{3dB} \rho \cdot L \sqrt{1 + \left(2 \frac{\rho}{\rho_0}\right)^2}}, \quad \rho_0 = \frac{\bar{\phi}_{3dB}}{6} D_A L \quad . \quad (15)$$

where $2\bar{\phi}_{3dB}$ is the azimuth half-power beamwidth. Once again, $R_{peak} \simeq 2$ has been assumed.

Evidently, as in (14), also in this case $\hat{S}_\rho(\rho, 0) \rightarrow D_A W_{rad} / 4\pi\rho^2$ as $\rho \rightarrow \infty$.

For arrays that exhibit a slight electrical down-tilt (typically 4-10 degrees), the prediction formulae (13), (15) maintain good accuracy at close distances in the array Fresnel region, where the radiation pattern has not yet established. The accuracy can be maintained at all distances and even in the far-field, provided the expressions are reformulated in a suitable reference frame defined by the direction of peak directivity in the elevation plane, as outlined in Appendix F.

As shown in [25], the formulae maintain good prediction accuracy also in the case of arrays that feature non-uniform feeding profiles, which are frequently employed to produce low side-lobe levels or particular ground illumination, e.g., cosecant-square elevation beams.

III.a Simplified expressions for the compliance distance

For a specific peak (\hat{S}) or average (\bar{S}) exposure limit, the corresponding compliance distance can be determined straightforwardly by inverting (13), (15), or (12), (E8) to determine ρ . The exact expressions, as well as analytically simpler, approximate expressions of the solutions are reported below

$$\bar{\rho} = \rho(\bar{S}) = \rho_0 \sqrt{\frac{\sqrt{1+4q^2}-1}{2}} \simeq \rho_0 \frac{q}{\sqrt[4]{1+q^2}} \quad , \quad (16a)$$

$$\hat{\rho} = \rho(\hat{S}) = \rho_0 \sqrt{\frac{\sqrt{1+64q^2}-1}{8}} \simeq \rho_0 \frac{2q}{\sqrt[4]{1+(4q)^2}} \quad , \quad (16b)$$

where the parameters ρ_0 and q are provided in Table I for omnidirectional and sector arrays.

Observe that the sector array parameters could have been derived from the corresponding expressions for omnidirectional arrays by formal substitution $\pi \rightarrow \bar{\phi}_{3dB}$; that is, except for the Gaussian shaping term. The same can be said for all the prediction formulae derived so far. Physically, it is as if the antenna radiates the RF power uniformly within an azimuth sector with

semi-aperture angle equal to $\bar{\phi}_{3dB}$ rather than π , as it would do for omnidirectional arrays.

The approximate expressions in (16) are plotted in Fig. 3a as a function of the parameter q . As seen in Fig. 3b, they introduce a slight conservative bias (about 8% overestimation at most) of the compliance distance in the near-field of the array, compared with the exact expressions. An additional conservative bias may be introduced if q is increased by a factor $\xi > 1$, which has the same effect as decreasing S . In doing so, the compliance distance would increase by the factor ξ in the array near-field, which is cylindrical in character, and by a factor $\sqrt{\xi}$ in the far-field, where the spherical field character induces sharper power density decay. This approach has been essentially adopted in a few instances, e.g., an Italian law regulating public exposure to electromagnetic fields [26] essentially established a factor $\xi = 2$ to allow the use of theoretical prediction methods in lieu of measurements. Notice that applying the factor ξ directly to the compliance distance (16) would be incorrect, as it would not account for the different field decay character near and far from the antenna, thus resulting in excessive additional bias in the antenna far-field.

III.b Discussion

The transition-point distance can be expressed in terms of the far-field compliance distance (ρ_∞ , as defined below) through the parameter q introduced earlier

$$\rho_0 = \rho_\infty / \sqrt{q}, \quad \rho_\infty = \begin{cases} \sqrt{\frac{W_{rad} D_A}{4\pi S}}, & \text{omnidirectional arrays} \\ \sqrt{\frac{W_{rad} D_A 2^{-(\phi/\bar{\phi}_{3dB})^2}}{4\pi S}}, & \text{sector arrays} \end{cases}, \quad (17)$$

so the compliance distance expressions (16) can be rewritten as follows

$$\bar{\rho} \approx \rho_{\infty} \sqrt[4]{\frac{q^2}{1+q^2}} \quad , \quad (18a)$$

$$\hat{\rho} \approx \rho_{\infty} \sqrt[4]{\frac{(4q)^2}{1+(4q)^2}} \quad , \quad (18b)$$

thus pointing out the functions describing the transition from the near-field cylindrical behavior of the array field to the far-field behavior. As a matter of fact, Eqs. (18) show how the parameter q incorporates nicely all the factors affecting the transition of the compliance distance from the cylindrical to the spherical propagation region, as well as their relative contribution. Obviously, the compliance distance increases with the radiated power W_{rad} and decreases with increasing power density limit S . The antenna length L and the azimuth beamwidth angle $\bar{\phi}_{3dB}$ are fairly independent parameters. From classical array theory, directivity (D_A) is inversely proportional to both azimuth and elevation beamwidths, while the electrical array length is inversely proportional to the latter. Therefore the parameter q is inversely proportional to L^3 ($\bar{\phi}_{3dB} L^3$ for sector arrays), thus leading to the otherwise intuitive conclusion that, everything else being the same, larger arrays allow closer compliance distances because of the corresponding decrease of the field energy density. Similarly, the compliance distance decreases with larger azimuth beamwidth ($\bar{\phi}_{3dB}$) because of correspondingly wider angular spread of RF energy. Notice that the above considerations hold unless the antennas exhibit different peak *EIRP* (*effective isotropic radiated power*, i.e., the product $W_{rad} \cdot D_A$), since *EIRP* appears in the expression of ρ_{∞} .

IV. VALIDATION OF THE PREDICTION FORMULAE

The prediction formulae for the peak equivalent power density were derived after establishing an upper bound for the peak to average power density versus distance. Therefore the parameter

$R_{peak} \simeq 2$, which was central to said derivation, will be verified first. Then, the accuracy of Eqs. (13), (15), enabling the peak power density prediction for omnidirectional and sector arrays, respectively, will be assessed. Finally, the accuracy of the simplified compliance distance equations (16) will be verified, also in the case of arrays featuring an electrical tilt of the main beam. Whenever applicable, the analysis will be presented using normalized distance units, the free-space wavelength being the normalizing factor.

IV.a Peak-to-average power density ratio

This analysis is aimed at establishing the accuracy of the parameter R_{peak} defined in (11) by evaluating numerically the field radiated by realistic array antennas. In so doing, we will also verify some of the intermediate steps leading to (11), such as the assumption that the absolute peak of the equivalent power density lay on the $z = 0$ mid-plane where the maximum relative phase swings between *GO* and diffracted field occur, and the consequent estimation of the peak distance (10). Therefore, in this analysis, two quantities are tracked. One is the power density peak-to-average ratio versus distance

$$R(\rho) = \frac{\max_{|z| < L/2} \{S_\rho(\rho, z)\}}{\text{avg}_{|z| < L/2} \{S_\rho(\rho, z)\}}, \quad (19)$$

and the other is the ratio between the power density at the array mid-plane ($z = 0$) and the average

$$M(\rho) = \frac{S_\rho(\rho, 0)}{\text{avg}_{|z| < L/2} \{S_\rho(\rho, z)\}}. \quad (20)$$

The Numerical Electromagnetic Code [27] was employed to derive all the results, after testing its accuracy with other two commercial moment-method codes: the General Electro-Magnetic code

(GEM) [28]-[29], and IE3D [30].

In particular, we have analyzed two omnidirectional collinear arrays, featuring five and eight half-wave resonant dipoles, respectively, and two five-element sector arrays (shown in Fig. 4), one vertically polarized and the other horizontally polarized. Following the notation introduced in Fig. 1, all arrays feature inter-element distance $\Delta = \lambda_0$, with the exception of the horizontally polarized sector array in Fig. 4b ($\Delta = 0.85\lambda_0$). The five-element omnidirectional array, of length $L = 4.5\lambda_0$, comprises equally fed collinear dipoles yielding peak directivity $D_A = 9.62 \text{ dBi}$ at broadside. The transition-point distance is $\rho_0 = 20.6\lambda_0$, while the peak distance is $\rho_{peak} = 8.1\lambda_0$. The eight-element collinear array length is $L = 7.5\lambda_0$, as it features equally fed dipoles yielding peak directivity $D_A = 11.76 \text{ dBi}$ at broadside. The transition-point distance is $\rho_0 = 56.2\lambda_0$, while the peak distance is $\rho_{peak} = 22.5\lambda_0$. The ratios $R(\rho)$ and $M(\rho)$ are plotted in Figs. 5a, 5b for the five-element and the eight-element array, respectively. As plot abscissas are normalized to ρ_{peak} , a vertical dotted line indicates $\rho = \lambda_0$, i.e., the lower validity bound of the prediction formulae. These results show the remarkable accuracy of Eqs. (10)-(11) in predicting distance from the antenna and amplitude of the power density peak. As shown by the convergence of the two ratios, it is also verified that the absolute peak actually occurs at the array mid-plane, as we had hypothesized on the basis of physically intuitive arguments. Such a finding further remarks the dominant role of the zero-th order current harmonic in establishing the fundamental characteristics of the field radiated by broadside collinear arrays.

The electrical dimensions of the five element sector arrays are provided in Fig. 4. In NEC, the metal reflector surfaces were modeled using a wire grid with $\lambda_0/20$ mesh size. The vertically polarized panel array exhibits 74-degree half-power azimuth beamwidth ($\bar{\phi}_{3dB} = 37^\circ$)

and peak directivity $D_A = 16.2 \text{ dBi}$ at broadside, yielding $\rho_0 = 22.4\lambda_0$ and $\rho_{peak} = 10\lambda_0$. Notice that the transition-point and peak distances obtained in this case are almost identical to those of the five-element omnidirectional array, even though there is an almost five-fold difference in directivity. Actually, the small difference in ρ_0 and ρ_{peak} can be wholly attributed to the different electrical length, which is about 10% larger for the sector array due to the back-panel. Looking at the expression for ρ_0 in Eq. (15), the five-fold directivity difference is compensated by the factor $\bar{\phi}_{3dB} / 6 \simeq 0.108$, which is about five times lower than the corresponding factor (0.5) in the ρ_0 expression for omnidirectional arrays (13). The physical interpretation to the above observation is based on the diffraction phenomena, whose impact on the array near-field behavior extends up to distances where the phase delay difference from different antenna current elements is still significant. Since the antenna geometry extends mainly in height, whereas its width is comparable with the field wavelength, the field transition processes towards the spherical wave-propagation regime are dominated by the diffraction at the array tips, i.e., by the array length, not by the azimuth distribution of RF energy. As a matter of fact, the relevance of the array length, above all other antenna parameters, was already implicit in the expression of ρ_{peak} (10), where the array length plays the only significant role. Notice that typically the difference in length between the active array elements and the reflector is kept small enough to limit the antenna to a reasonable size and achieve at the same time the desired pattern front-to-back ratio. The reflector's current produces a significant diffractive contribution to the total field when the physical truncation affects its currents significantly. Should the back-plane extend further, its diffractive effect in the broadside direction would reduce because the currents would be less perturbed. In this case, it is to be expected that the mirroring function performed by the back-plane would be more effective, meaning that the antenna behaves more as if the radiation process is due to the

active elements and their mathematical images. Therefore, the effective antenna length would get closer to the physical length of the active element array and the reflector's dimensions would play a lesser role.

The horizontally polarized panel array exhibits 60-degree half-power azimuth beamwidth ($\bar{\phi}_{3dB} = 30^\circ$) and peak directivity $D_A = 16.44 \text{ dBi}$ at broadside, yielding $\rho_0 = 15.4\lambda_0$ and $\rho_{peak} = 6.4\lambda_0$. In this case it is even more evident that the array length plays the central role in determining the fundamental antenna characteristics, even though the current polarization is orthogonal to the antenna's largest dimension, i.e., its length.

The accuracy of the Gaussian shaping function (E4) describing the azimuth dependence of the array pattern can be inferred from Fig. 6, showing excellent agreement along directions $\phi \leq \bar{\phi}_{3dB}$. Accuracy degrades rapidly for $\phi > 1.5\bar{\phi}_{3dB}$, because the Gaussian profile fails to describe the sideways energy spread due to edge diffraction effects. However, such a discrepancy is of no concern and is well worth the analytical simplicity that (E4) provides to (15), as the directions $\phi \leq \bar{\phi}_{3dB}$ are those of practical interest for compliance assessments. Other profiles, analytical or interpolated from pattern data, can always be employed as shown in Appendix E to improve accuracy, if one so desires.

In Fig. 7 we report the ratios $R(\rho)$ and $M(\rho)$, for the vertically polarized and the horizontally polarized sector arrays, respectively. Once again, we observe a remarkable agreement with the predictions of Eqs. (10)-(11). Also for sector arrays, the absolute peak occurs at the antenna mid-plane, as shown by the convergence of the two ratios about $\rho = \rho_{peak}$.

A common behavior is observed in all the cases analyzed in Figs. 5 and 7, in that the power density peaks around ρ_{peak} at about twice the average, and then starts its monotonic de-

cay. Said peak is not exceeded at distances closer to the array, except in the reactive near-field of the array elements ($\rho < \lambda_0$), where exposure should be assessed on the basis of SAR.

IV.b Accuracy of the power density prediction formulae

The aim of this analysis is to provide an example of the prediction error that would be experienced applying the peak and average power density prediction formulae to the array antennas introduced earlier. The error is counted positive if the prediction formulae overestimate the actual exposure level, as computed using NEC. In Fig. 8 we report the prediction error for the five and eight-element collinear arrays, in the broadside direction where the aeriels exhibit peak gain. The corresponding results for the sector arrays are presented in Fig. 9. Peak and average power density converge asymptotically, providing an overestimate of the exposure in the array near-field except for a slight underestimation around the transition-point distance ρ_0 . In all cases, the overestimate is more pronounced for the peak power density.

As expected, the omnidirectional array formulae provide an exact prediction in the far-field, whereas the sector array formulae preserve a 0.2 dB asymptotic error due to the approximations introduced in Eq. (E8) ($\pi/3|_{dB} \approx 0.2\text{ dB}$). The asymptotic error may vary with the azimuth angle due to the additional error introduced using the Gaussian function to describe the azimuth pattern variation, as shown in Fig. 10 for the vertically polarized sector array. The prediction error for $\phi = 30^\circ$ converges to about 0.25 dB asymptotically; the extra 0.05 dB is provided by the slight overestimate of the Gaussian function (see Fig. 6). On the other hand, for $\phi = 60^\circ$, the asymptotic error is about -0.8 dB , due to the 1 dB underestimation produced by the Gaussian function in that direction (see Fig. 6). At distances from the antenna closer than one wavelength, a region dominated by reactive energy, the formulae provide inaccurate results.

IV.c Accuracy of the prediction formulae for the compliance distance

As mentioned earlier, the simplified compliance distance expressions (16) introduce a slight overestimate ($\sim 8\% \Rightarrow \sim 0.3$ dB) compared with the exact expressions that would be derived by inverting the power density prediction formulae. It turns out that such an overestimate occurs mainly around the transition-point distance, and has the net effect of compensating almost exactly the slight underestimation produced by the power density prediction formulae about that distance. This favorable feature can be observed in the results reported in Figs. 11 and 12 for the omnidirectional and sector arrays, respectively. In the figures, the compliance distance is plotted versus the parameter q introduced earlier. A very good agreement between predicted and actual compliance distance can be observed in all cases. Thanks to the slight conservative bias they introduce, the prediction formulae (16) always overestimate the actual compliance distance. The overestimation vanishes at large distance. In the array near-field, the prediction formulae for $\hat{\rho}$ describe an envelope to the actual, rather complicated behavior. The formulae for $\bar{\rho}$ introduce only a slight overestimation in the near-field.

All the above-mentioned characteristics are favorable features of the compliance distance prediction formulae (16). In the array near-field, where it is more likely that scattering from the floor and nearby objects may perturb the array field, larger overestimation is introduced by the prediction formulae. Smaller overestimation is introduced moving towards the transition-point distance and then the far-field, as scattering effects are less likely to occur. For instance, an rooftop installation may feature the antenna mounted a few meters from the edge of the building, and maintenance personnel may have access to the area in front the antenna, i.e., in its near-field. On the other hand, windows in nearby buildings that may be facing the installation are in the array

far-field. Finally, observe that a lesser degree of overestimation is introduced on $\bar{\rho}$ compared to $\hat{\rho}$, which reflects the fact that the average is more robust than the spatial-peak power density with respect to scattering in the array near-field.

IV.d Accuracy of the prediction formulae for electrically tilted beam arrays

The prediction formulae derived in Appendix F, relative to arrays whose main beam is electrically down-tilted so as to produce a desired ground illumination, will be verified with an eight-element omnidirectional array. Figure 13 displays the reference frame defined by the array beam down-tilt angle γ . The array has the characteristics described earlier, except for a 60-degree progressive phase shift between feeds that produces a $\gamma = 9.5^\circ$ down-tilt of the main beam, with peak directivity $D_A = 11.15 \text{ dBi}$. The transition-point is $r_0 = 47.5 \lambda_0$. For brevity's sake, in Fig. 14 we only report the comparison between predicted and exact compliance distance. The comparison is carried out for distances greater than one wavelength along the beam peak direction γ . In the computations, we have discarded intercepting conical surfaces that get within one wavelength from the array axis ($\Delta\rho < \lambda_0$ in Fig. 13), effectively starting the computation at a distance

$$r_\gamma = \frac{\lambda_0}{\cos \gamma} + \frac{L}{2} \sin |\gamma| \quad . \quad (21)$$

From Fig. 14, we observe that both prediction formulae provide the desired conservative bias at distances greater than $r_\gamma \simeq 1.6 \lambda_0$.

V. CONCLUDING REMARKS

The peak power density prediction formulae derived in this paper, combined with those for the average power density derived in [21], can be employed to perform compliance assessment near

base-station antennas with respect to both IEEE and ICNIRP RF safety guidelines. It may be appreciated that the analytical complexity of the peak power density formulae has not increased, compared with the average power density formulae, even though the behavior of the physical quantity they describe is far more complicated. They are based on a cylindrical propagation model of the array near-field, which was rigorously demonstrated for collinear arrays and extensively verified also for arbitrarily polarized sector arrays, including those featuring non uniform feeding profiles [21]-[22], [25].

The prediction formulae have a built-in conservative bias in order to yield an overestimation of the actual exposure levels, which is desirable for compensating perturbations due to the environment, e.g., floor reflections. The formulae are applicable to broadside arrays regardless of the feeding profile of its elements, as long as the array exhibits a single main beam. As discussed in Appendix F, it is possible to use them even for arrays whose radiation beam is electrically down-tilted, provided they are reformulated in a suitable reference frame.

Some basestation antennas may exhibit dual polarization. Since the accuracy of the prediction formulae presented herein has been verified for vertically and horizontally polarized arrays, they allow the analysis of dual polarized antennas as well.

In the near future, smart antenna and MIMO (*multiple-input multiple-output*) techniques will be implemented at basestation to increase infrastructure capacity. These techniques produce variable antenna beams that are generated adaptively to respond to changing electromagnetic environment and mobile transceiver's position. The RF safety compliance near such installations will certainly present a challenge, as well as an interesting research topic, if overly conservative assessments are to be avoided.

Finally, let us remark that, regardless of the array size, at distances closer than one wavelength from the array the reactive field is dominant due to the proximity to the individual radiat-

ing elements. In such a case, the near-field coupling of exposed subjects with the RF source should be assessed by means of *specific absorption rate* (SAR) measurements, e.g., in human-like shaped phantoms. That is the case, for instance, of the exposure to wireless handsets [4]. Even though the likelihood of requiring compliance assessments at such short distances is quite slim in the case of outdoor basestation installations, it may become necessary in the case of low-power pico-cell infrastructure for voice and data, which may utilize hub stations in environments that do not allow enforcement of compliance distances, e.g., installing fences, easily. There will be a need to define standard SAR assessment procedures, similar to those employed in [31], for this kind of operating conditions.

REFERENCES

- [1] IEEE Std C95.1-1999. IEEE Standard for Safety Levels with Respect to Human Exposure to RF Electromagnetic Fields, 3 kHz to 300 GHz.
- [2] International Commission on Non-Ionizing Radiation Protection (ICNIRP), "Guideline for Limiting Exposure to Time-Varying Electric, Magnetic, and Electromagnetic Fields," *Health Physics*, vol. 74, no. 4, pp. 494-522, April 1998.
- [3] C. K. Chou, H. Bassen, J. Osepchuk, Q. Balzano, R. Petersen, M. Meltz, R. Cleveland, J. C. Lin, L. Heynick, "Radio frequency electromagnetic exposure: Tutorial review on experimental dosimetry," *Bioelectromagnetics*, vol. 17, no. 3, pp. 195-208, 1996.
- [4] Q. Balzano, O. Garay, and T. J. Manning, Jr., "Electromagnetic energy exposure of simulated users of portable cellular telephones," *IEEE Trans. on Veh. Tech.*, vol. 44, no. 3, pp. 390-403, Aug. 1995.
- [5] Federal Communications Commission, OET Bulletin 65, "Evaluating compliance with FCC guidelines for human exposure to radio-frequency electromagnetic fields," Ed. 97-01, 1997.
- [6] IEEE Std C95.3-2002 IEEE Recommended Practice for Measurements and Computations of Radio Frequency Electromagnetic Fields with Respect to Human Exposure to Such Fields, 100 kHz-300 GHz.
- [7] C. Olivier and L. Martens, "A practical method for compliance testing of base stations for mobile communications with exposure limits," *Proc. of the 2001 IEEE International Symp. of the Antennas and Propagation Society*, Vol. 2, pp. 64-67, Boston, MA, July 2001.
- [8] S. Blanch, J. Romeu, and A. Cardama, "Near field in the vicinity of wireless base-station antennas: an exposure compliance approach," *IEEE Transactions on Antennas and Propagation*, Vol. 50, No. 5, pp. 685-692, May 2002.

- [9] M. Bizzi and P. Gianola, "Electromagnetic fields radiated by GSM antennas, *Electronics Letters*, Vol. 35, No. 11, pp. 855–857, 27 May 1999.
- [10] C. Olivier and L. Martens, "A more accurate method to define exclusion zones," *Proc. of the Radio and Wireless Conference (RAWCON) 2000*, pp. 107-110, 2000.
- [11] Z. Altman, B. Begasse, C. Dale, A. Karwowski, J. Wiart, M. Wong, L. Gattoufi, "Efficient models for base station antennas for human exposure assessment," *IEEE Transactions on Electromagnetic Compatibility*, Vol. 44, No. 4, pp. 588- 592, Nov. 2002.
- [12] S. A. Hanna, "On human exposure to radio-frequency fields around transmit radio sites," *Proc. of the 1999 IEEE International Symposium of the Vehicular Technology Society*, Vol. 2, pp. 1589 -1593, 1999.
- [13] M. Barbiroli, C. Carciofi, G. Falciasacca, M. Frullone, "Analysis of field strength levels near base station antennas," *Proc. of the 1999 IEEE International Symposium of the Vehicular Technology Society*, Vol. 1, pp. 156 -160, 1999.
- [14] L. Catarinucci, P. Palazzari, and L. Tarricone, "Human exposure to the near field of radio-base antennas—A fullwave solution using parallel FDTD," *IEEE Transactions on Microwave Theory and Techniques*, Vol. 51, No. 3, pp. 935–940, March 2003.
- [15] G. Lazzi and O. P. Gandhi, "A mixed FDTD-integral equation approach for on-site safety assessment in complex electromagnetic environments," *IEEE Transactions on Antennas and Propagation*, Vol. 48, No. 12, pp. 1830–1836, Dec. 2000.
- [16] O. P. Gandhi and M. S. Lam, "An On-Site Dosimetry System for Safety Assessment of Wireless Base Stations Using Spatial Harmonic Components," *IEEE Transactions on Antennas and Propagation*, Vol. 51, No. 4, pp. 840–847, Apr. 2003.
- [17] D. Lautru, J. Wiart, W. Tabbara, R. Mittra, "A MoMTD/FDTD hybrid method to calculate the SAR induced by a base station antenna," *Proc. of the 2000 IEEE International Sympo-*

sium of the Antennas and Propagation Society, Vol. 2, pp. 757 -760, 2000.

- [18] P. Bernardi, M. Cavagnaro, S. Pisa, and E. Piuze, "Human exposure to radio base-station antennas in urban environment," *IEEE Trans. on Microwave Theory Tech.*, vol. 48, No. 11, pp. 1996-2002, Nov. 2000.
- [19] P. Bernardi, M. Cavagnaro, S. Pisa, and E. Piuze, "Evaluation of human exposure in the vicinity of a base-station antenna using the multiple-region/FDTD hybrid method," *Micro-wave Symposium Digest, 2002 IEEE MTT-S International Symposium*, Vol. 3, pp. 1747 – 1750, 2002.
- [20] A. M. Martinez-Gonzalez, A. Fernandez-Pascual, E. de los Reyes, W. Van Loock, C. Gabriel, and D. Sanchez-Hernandez, "Practical Procedure for Verification of Compliance of Digital Mobile Radio Base Stations to Limitations of Exposure of the General Public to Electromagnetic Fields," *IEE Proc. Microw. Antennas Propag.*, vol, 149, No. 4, pp. 218-228, Aug. 2002.
- [21] A. Faraone, R. Tay, K. Joyner, and Q. Balzano, "Estimation of the Average Power Density in the Vicinity of Cellular Base Station Antennas," *IEEE Trans. on Vehicular Technology*, Vol. 49, No. 3, pp. 984-996, May 2000.
- [22] R. Cicchetti, A. Faraone, and Q. Balzano, "A Uniform Asymptotic Evaluation of the Field Radiated from Collinear Array Antennas," *IEEE Transactions on Antennas and Propagation*, Vol. 51, No. 1, pp. 89-102, Jan. 2003.
- [23] R. C. Petersen and P. A. Testagrossa, "Radio-Frequency Electromagnetic Fields Associated with Cellular-Radio Cell-Site Antennas," *Bioelectromagnetics*, 13, pp. 527-542, 1992.
- [24] R. A. Tell, "Engineering Services for Measurement and Analysis of Radiofrequency (RF) Fields," Richard Tell Associates, Inc. Las Vegas, NV. Federal Communication Commission (FCC) Report No. OET/RTA 95-01, June 1995.

- [25] Q. Balzano and A. Faraone, "Peak and Average RF Safety Compliance Levels near Radio Base Station Antennas - Prediction Formulas and Numerical Validation," *Proc. IEEE Intl. Symposium on Electromagnetic Compatibility*, pp. 780-785, Montreal, Canada, Aug. 13-17, 2001.
- [26] Italian Government Decree 10 September 1998, no. 381, published on the Italian Official Gazette (*Gazzetta Ufficiale*), 3 November 1998, no. 257.
- [27] NEC-Win PRO TM v 1.1, Nittany Scientific, Inc., Riverton, UT.
- [28] General Electromagnetic code (GEM) 12.0, AMEL, Inc., Boulder, CO.
- [29] B. M. Notaros, B. D. Popovic, J. P. Weem, R. A. Brown, and Z. Popovic, "Efficient Large-Domain MoM Solutions to Electrically Large Practical EM Problems," *IEEE Trans. on Microwave Theory Tech.*, Vol. 49, No. 1, pp. 151-159, Jan. 2001.
- [30] IE3DTM v7.0. Zeland Software Inc., Fremont, CA.
- [31] J. Cooper, B. Marx, J. Buhl, and V. Hombach, "Determination of safe distance limits for a human near a cellular base station antenna, adopting the IEEE standard or ICNIRP guidelines," *Bioelectromagnetics*, Vol. 23, pp. 429-443, Sept. 2002.

APPENDIX A. THE ARRAY FIELD AND ITS ASYMPTOTIC REPRESENTATION

The electromagnetic field radiated by an arbitrary collinear array antenna may be computed by integrating the free-space dyadic Green's function with the traveling wave representation of the current distribution excited along the antenna axis. Such a representation, which has been chosen so as to allow a global analysis of the array field characteristics [22], is obtained in terms of spatial Fourier harmonics referred to the reference frame defined in Fig. 1

$$I(z) = I_0 + \sum_{n=1}^{\infty} \left(I_n^+ e^{-j\beta_n z} + I_n^- e^{+j\beta_n z} \right), \quad \beta_n = n \frac{2\pi}{L}, \quad |z| < \frac{L}{2}, \quad (A1)$$

where L is the antenna length. In (A1), I_0 is the current amplitude of the zero-*th* order spatial harmonic, i.e., the average value of the total current, I_n^+ and I_n^- are the *n-th* traveling wave current amplitudes, and β_n is the corresponding spatial wavenumber. The exact array field, is expressed in terms of propagating and evanescent Truncated Floquet Waves (*TFWs*) that are obtained by integrating the current distribution (A1) with the free-space dyadic Green's function

$$E_v(\mathbf{r}) = I_0 E_{v,0}(\mathbf{r}) + \sum_{n=1}^{\infty} \left[I_n^+ E_{v,n}^+(\mathbf{r}) e^{-j\beta_n z} + I_n^- E_{v,n}^-(\mathbf{r}) e^{+j\beta_n z} \right], \quad (v = \rho, z) \quad (A2)$$

$$H_{\phi}(\mathbf{r}) = I_0 H_{\phi,0}(\mathbf{r}) + \sum_{n=1}^{\infty} \left[I_n^+ H_{\phi,n}^+(\mathbf{r}) e^{-j\beta_n z} + I_n^- H_{\phi,n}^-(\mathbf{r}) e^{+j\beta_n z} \right] \quad (A3)$$

where $E_{v,n}^{\pm}(\mathbf{r})$, and $H_{\phi,n}^{\pm}(\mathbf{r})$, are the *n-th* spatial Floquet harmonics defining the electric and magnetic field distribution, respectively [22]. This field representation applies in general to non-uniform collinear arrays, and simplifies if the current distribution is symmetric (broadside arrays) or anti-symmetric. As shown in [22], Truncated Progressive Floquet waves (*TPFWs*) generate the main beam (zero-*th* order harmonic) and the secondary beams, while Truncated Evanescent Floquet Waves (*TEFWs*) represent the reactive field responsible for the energy storage

near the array axis. The field is expressed in terms of *GO* and diffracted ray-fields. The *GO* field is responsible for the cylindrical wave character observed in the array near-field, while the diffracted field produces the transition toward the spherical wave-propagation regime.

APPENDIX B. DEFINITION OF THE TRANSITION FUNCTION

The transition function employed in the expressions of the electromagnetic field produced by the fundamental as well as by the higher current harmonics is defined as follows

$$F_t(\zeta) = 2e^\zeta \sqrt{\zeta} \int_{\sqrt{\zeta}}^{\infty} e^{-\tau^2} d\tau \quad , \quad (\text{B1})$$

with the principal value of the square root defined with the branch-cut along the negative real-axis. This function, responsible for the field transition toward the spherical wave-propagation regime, assures the required continuity of the total electromagnetic field across the shadow boundaries of the *GO* field [22]. The function $F_t(\zeta)$ has the following asymptotic representations

$$F_t(\zeta) \sim \begin{cases} \sqrt{\pi\zeta} e^\zeta - \sum_{k \geq 0} \frac{(2\zeta)^{k+1}}{\prod_{0 \leq h \leq k} (2h+1)} , & \zeta \rightarrow 0 \\ 1 - \frac{1}{2\zeta} , & \zeta \rightarrow \infty . \end{cases} \quad (\text{B2})$$

APPENDIX C. POWER RADIATED FROM THE ZERO-TH ORDER CURRENT HARMONIC

The real power radiated from a thin current filament of length L , excited by a current of amplitude I_0 , is computed by integrating the equivalent power density over a closed sphere located in the far-field, where the electromagnetic field components are expressed in spherical coordinate as follows

$$E_{\theta}(\mathbf{r}) \underset{r \rightarrow \infty}{\sim} j\beta\eta_0 g_0(r) I_0 L \operatorname{sinc}\left(\beta \frac{L}{2} \cos \theta\right) \sin \theta, \quad (\text{C1})$$

$$H_{\phi}(\mathbf{r}) \underset{r \rightarrow \infty}{\sim} j\beta g_0(r) I_0 L \operatorname{sinc}\left(\beta \frac{L}{2} \cos \theta\right) \sin \theta, \quad (\text{C2})$$

where $g_0(r)$ is the free-space Green's function, η_0 is the free-space wave impedance, $\beta = 2\pi / \lambda_0$ is the free-space wavenumber, and $\operatorname{sinc}(\zeta) = \sin \zeta / \zeta$. The corresponding distribution of the spatial power density is

$$S_r(\mathbf{r}) \underset{r \rightarrow \infty}{\sim} \frac{\eta_0}{2} \beta^2 \left(\frac{|I_0| L}{4\pi r} \right)^2 \operatorname{sinc}^2 \left[\beta \frac{L}{2} \cos \theta \right] \sin^2 \theta, \quad (\text{C3})$$

so that the radiated power W_{rad} , found by integration over a sphere, is

$$W_{rad} = \eta_0 \frac{\beta L \cos \beta L + \sin \beta L - 2\beta L + \beta^2 L^2 \operatorname{Si}(\beta L)}{4\pi\beta L} |I_0|^2. \quad (\text{C4})$$

The *sine integral* function $\operatorname{Si}(\zeta)$ in (C4) has the following large-argument asymptotic representation

$$\operatorname{Si}(\zeta) = \int_0^{\zeta} \frac{\sin \tau}{\tau} d\tau \underset{\zeta \rightarrow \infty}{\sim} \frac{\pi}{2} - \frac{\cos \zeta}{\zeta}. \quad (\text{C5})$$

Using (C5), we can determine the asymptotic limit for the radiated power from a large current filament

$$W_{rad} \underset{\beta L \rightarrow \infty}{\sim} \eta_0 \frac{\beta L}{8} |I_0|^2. \quad (\text{C6})$$

It is extremely interesting to notice that (C6) coincides with the real power flow, across a cylinder of length L coaxial with the array, due to the *GO* field alone [22]. Therefore, the average power density of the *cylindrical GO* field is

$$S_{cyl}^{GO}(\rho) = \frac{W_{rad}}{2\pi\rho L} = \eta_0\beta \frac{|I_0|^2}{16\pi\rho} \quad . \quad (C7)$$

It can be easily verified that (C7) gives a good approximation of the power density radiated by a current line with $L/\lambda_0 \geq 4$.

APPENDIX D. DERIVATION OF THE PEAK DISTANCE

Equation (9) is rewritten in terms of *normalized* dimensions (indicated by the tilde) as follows

$$\tilde{T}(\tilde{\rho}, 0) = 1 + \left(\frac{2}{\pi\tilde{L}} \right)^2 \tilde{\rho} \left(\frac{\tilde{\rho}}{\tilde{r}} \right)^3 - \sqrt{\tilde{\rho}} \left(\frac{\tilde{\rho}}{\tilde{r}} \right) \frac{2}{\pi\tilde{L}} \left\{ e^{j\left[2\pi(\tilde{r}-\tilde{\rho})+\frac{\pi}{4}\right]} + \left(\frac{\tilde{\rho}}{\tilde{r}} \right) e^{-j\left[2\pi(\tilde{r}-\tilde{\rho})+\frac{\pi}{4}\right]} \right\} \quad (D1)$$

where $\tilde{\rho} = \rho/\lambda_0$, $\tilde{r} = r/\lambda_0$, and $\tilde{L} = L/\lambda_0$. For moderate size arrays ($\tilde{L} \geq 2$), the first-order estimate for the peak distance provided by Eq. (37) in [22] is $\tilde{\rho}_{peak} \simeq \tilde{L}^2/3$. The real part of (D1) is found as follows

$$\tilde{T}_R(\tilde{\rho}, \tilde{L}) = \frac{\tilde{T}(\tilde{\rho}, \tilde{L}) + \tilde{T}(\tilde{\rho}, \tilde{L})^*}{2} = 1 + \frac{4}{\pi^2} \frac{\tilde{\rho}}{\tilde{L}^2} \left(\frac{\tilde{\rho}}{\tilde{r}} \right)^3 - \frac{2}{\pi} \sqrt{\frac{\tilde{\rho}}{\tilde{L}^2}} \frac{\tilde{\rho}}{\tilde{r}} \left(1 + \frac{\tilde{\rho}}{\tilde{r}} \right) \cos \left[2\pi(\tilde{r} - \tilde{\rho}) + \frac{\pi}{4} \right] \quad (D2)$$

Since we are interested in finding the location of the main peak of this function, we can approximate the slowly varying function $\tilde{\rho}/\tilde{r} \simeq 1$, and rewrite the argument of the cosine making the following approximation

$$\tilde{r} - \tilde{\rho} = \tilde{\rho} \sqrt{1 + \left(\frac{\tilde{L}}{2\tilde{\rho}} \right)^2} - \tilde{\rho} \simeq \tilde{\rho} \left[1 + \frac{1}{2} \left(\frac{\tilde{L}}{2\tilde{\rho}} \right)^2 \right] - \tilde{\rho} = \frac{\tilde{L}^2}{8\tilde{\rho}} \quad , \quad (D3)$$

thereby obtaining the following function

$$\tau(\tilde{\rho}, \tilde{L}) = 1 + \frac{4}{\pi^2} \frac{\tilde{\rho}}{\tilde{L}^2} - \frac{4}{\pi} \sqrt{\frac{\tilde{\rho}}{\tilde{L}^2}} \cos \left(\frac{\pi}{4} \frac{\tilde{L}^2}{\tilde{\rho}} + \frac{\pi}{4} \right) \quad , \quad (D4)$$

which can be used to estimate the location of the peak. Notice that (D4) can be written as a function of the variable $\chi = \sqrt{\tilde{\rho}/\tilde{L}^2}$ as follows

$$\tau(\chi) = 1 + \frac{4}{\pi^2} \chi^2 - \frac{4}{\pi} \chi \cos\left(\frac{\pi}{4\chi^2} + \frac{\pi}{4}\right) \quad . \quad (\text{D5})$$

The first-order estimate of the peak distance in [22] (corresponding to $\chi = \sqrt{1/3}$) was determined by enforcing the cosine's argument to be equal to π , therefore we can expand the cosine about π as follows

$$\tau(\chi) \simeq 1 + \frac{4}{\pi^2} \chi^2 - \frac{4}{\pi} \chi \left[-1 + \frac{1}{2} \left(\frac{\pi}{4\chi^2} + \frac{\pi}{4} - \pi \right)^2 \right] \quad , \quad (\text{D6})$$

yielding the following analytical condition for its derivative

$$\tau'(\chi) \simeq \frac{\left(\frac{4}{\pi} - \frac{9\pi}{8} + \frac{8\chi}{\pi^2} \right) \chi^4 - \frac{3\pi}{4} \chi^2 + \frac{3\pi}{8}}{\chi^4} = 0 \quad . \quad (\text{D7})$$

Notice that we expressed the numerator in (D7) in biquadratic form, with the highest-order coefficient showing a weak dependence on χ in the surroundings of $\chi = \sqrt{1/3} = 0.577$, where we expect to find the solution. Because of this weak dependence, we can substitute this starting value into said coefficient and obtain the following biquadratic equation

$$\left(\frac{4}{\pi} - \frac{9\pi}{8} + \frac{8}{\pi^2} \sqrt{\frac{1}{3}} \right) \chi^4 - \frac{3\pi}{4} \chi^2 + \frac{3\pi}{8} = 0 \quad , \quad (\text{D8})$$

which can be solved analytically yielding the real and positive solution $\chi_{peak} = 0.622$, corresponding to $\tilde{\rho}_{peak} = 0.386 \tilde{L}^2$, thus leading to Eq. (10). Notice that this value, being close to the first order approximation presented in [22], legitimizes the approximations used to derive Eqs. (D3), (D6), and (D8).

APPENDIX E. AVERAGE POWER DENSITY PREDICTION FORMULA FOR SECTOR ARRAYS

At distances closer than the transition-point ρ_0 , the power flow is essentially confined in the cylinder enclosing the array antenna, so the average power density can be written as

$$\bar{S}_\rho(\rho, \phi) = \frac{W_{rad}}{2\pi\rho L} \Phi(\phi), \quad -\frac{L}{2} < z < \frac{L}{2}, \quad (E1)$$

where the function $\Phi(\phi)$, describing the azimuth pattern variation, must obey the following constraint if all the real power is to flow through the lateral cylinder surface

$$\int_{-L/2}^{L/2} dz \int_{-\pi}^{\pi} \bar{S}(\rho, \phi) \rho d\phi = W_{rad} \Rightarrow \int_{-\pi}^{\pi} \Phi(\phi) d\phi = 2\pi. \quad (E2)$$

In general, we can assume the azimuth variation in the form $\Phi(\phi) = \Phi_0 \psi(\phi)$, with the condition $\psi(0) = 1$, where

$$\Phi_0 = \frac{2\pi}{\int_{-\pi}^{\pi} \psi(\phi) d\phi}. \quad (E3)$$

A good representation of the azimuth variation for antennas exhibiting a single main lobe at broadside is provided by the *Gaussian* profile

$$\psi(\phi) = 2^{-(\phi/\bar{\phi}_{3dB})^2}, \quad -\pi < \phi < \pi, \quad (E4)$$

where $\pm\bar{\phi}_{3dB}$ is the half-power horizontal beamwidth, which, for $\bar{\phi}_{3dB} < \pi/2$, yields

$$\Phi_0 \simeq \frac{2\sqrt{\pi \ln 2}}{\bar{\phi}_{3dB}} \simeq \frac{3}{\bar{\phi}_{3dB}}. \quad (E5)$$

The prediction formula for the average power density, incorporating the transition function from cylindrical to spherical propagation regime [21], becomes

$$\bar{S}_\rho(\rho, \phi) = \frac{W_{rad} \Phi(\phi)}{2\pi\rho \cdot L \sqrt{1 + \left(\frac{\rho}{\rho_0}\right)^2}} = \frac{W_{rad} 2^{-(\phi/\bar{\phi}_{3dB})^2}}{\frac{2}{3} \bar{\phi}_{3dB} \pi \rho \cdot L \sqrt{1 + \left(\frac{\rho}{\rho_0}\right)^2}} \quad . \quad (E6)$$

The transition-point ρ_0 is found by enforcing that the power density (E6) along broadside converge to its far-field expression

$$\bar{S}_\rho(\rho, 0) \underset{\rho \rightarrow \infty}{=} \frac{W_{rad} D_A}{4\pi\rho^2} \Rightarrow \rho_0 = \frac{\bar{\phi}_{3dB}}{6} D_A L \quad . \quad (E7)$$

where D_A is the antenna broadside directivity. Notice that directivity is employed here instead of the gain, as we did in [21] where we had assumed lossless radiators. The effects of ohmic and mismatch losses can be straightforwardly incorporated in the prediction formulae by writing W_{rad} as a function of the antenna efficiency. For all practical purposes, (E6) can be simplified ($\pi/3 \simeq 1$) further as follows

$$\bar{S}_\rho(\rho, \phi) = \frac{W_{rad} 2^{-(\phi/\bar{\phi}_{3dB})^2}}{2\bar{\phi}_{3dB} \rho \cdot L \sqrt{1 + \left(\frac{\rho}{\rho_0}\right)^2}}, \quad \rho_0 = \frac{\bar{\phi}_{3dB}}{6} D_A L \quad . \quad (E8)$$

Unlike the expressions previously proposed in [21], (E8) does not require knowledge of the array antenna reflector angle, but only readily available antenna parameters. Also notice that (E8) is equivalent to the expression proposed and numerically validated in [25], provided the aforementioned approximation is made.

APPENDIX F. PREDICTION FORMULA FOR ELECTRICALLY TILTED ARRAYS

To some extent, electrical beam downtilt can be interpreted as the physical tilt of an equivalent, shorter, broadside array, as shown in Fig. 13. For an omnidirectional array, we can determine the baseline for the *average* power density dividing the total radiate power by the intercepting sur-

face that in this case is conical rather than cylindrical. Based on the notations of Fig. 13, we obtain

$$\bar{S}_r(r, \gamma) = \frac{W_{rad}}{2\pi\rho \cdot L \cos \gamma} = \frac{W_{rad}}{2\pi r \cdot L \cos^2 \gamma}, \quad (\text{F1})$$

where γ is the beam tilt angle. Notice that another possible choice for the intercepting surface is represented by the cylindrical surface indicated in Fig. 13, which is orthogonal to the terrain, so measurements would most likely be carried out across that surface. Real power trough either surface is identical in the array far-field. We chose the conical surface since it provides a conservative bias in the power density estimate due to the smaller averaging surface.

As done in [21], enforcing the constraint that the average power density eventually coincide with its far-field expression, we obtain

$$\bar{S}_r(r, \gamma) = \frac{W_{rad}}{2\pi r \cdot L \cos^2 \gamma \sqrt{1 + \left(\frac{r}{r_0}\right)^2}}, \quad r_0 = D_A \frac{L}{2} \cos^2 \gamma, \quad (\text{F2})$$

Notice how the transition-point may become significantly closer then for broadside arrays, due to the shorter antenna aperture when looking from the direction of peak directivity. This effect is more pronounced the greater the tilt angle. It further indicates that the transition to the spherical propagation regime occurs even earlier for the secondary lobes of the array pattern. This is an interesting consideration, as it suggests that the exposure to the field emitted by the secondary lobes of basestation antennas, which typically occurs at ground level near the base of their masts or in nearby buildings, may be readily predicted neglecting the antenna aperture by means of the simple spherical propagation model.

Also in this case, the *peak* power density prediction formula can be derived by introducing the $R_{peak} \simeq 2$ magnification factor, as follows

$$\hat{S}_r(r, \gamma) \simeq \frac{W_{rad}}{\pi r \cdot L \cos^2 \gamma \sqrt{1 + \left(2 \frac{r}{r_0}\right)^2}}, \quad r_0 = D_A \frac{L}{2} \cos^2 \gamma. \quad (\text{F3})$$

The formal similarity between these expressions and (12), (13), upon substituting $L \rightarrow L \cos^2 \gamma$, suggests that the corresponding compliance distance can be predicted by means of the following formulae, formally identical to (16a) and (16b)

$$\bar{r} = r(\bar{S}) \simeq r_0 \frac{q}{\sqrt[4]{1 + q^2}}, \quad (\text{F4a})$$

$$\hat{r} = r(\hat{S}) \simeq r_0 \frac{2q}{\sqrt[4]{1 + (4q)^2}}, \quad (\text{F4b})$$

with

$$q = \frac{W_{rad}}{\pi (L \cos^2 \gamma)^2 D_A S}. \quad (\text{F5})$$

The prediction formulae for tilted array just derived do not take into account the formation of grating lobes near *endfire*, whose power content typically becomes significant for tilt angles greater than 10° . Hence, we delimit conventionally the validity of these formulae to the range $|\gamma| \leq 10^\circ$.

For brevity's sake, the corresponding expressions for sector arrays are not presented here, as they can be easily derived following the approach outlined in Appendix E.

FIGURE CAPTIONS

- Fig. 1 Broadside collinear array of half-wave dipoles and associated reference frame.
- Fig. 2 Fluctuation of the interference term for different electrical length of the antenna. The value of the peak overshoot converges rapidly to (11) as the length is increased.
- Fig. 3 Normalized compliance distance for peak and average power density limits; (a) transition from near to far-field as a function of the parameter q for the simplified expressions, and (b) overestimate they introduce compared to the exact solutions in (16).
- Fig. 4 Reflector-backed sector arrays comprising five half-wave dipole elements; (a) vertically polarized, and (b) horizontally polarized.
- Fig. 5 Fluctuating behavior along broadside of the peak and mid-plane power density ratios versus average power density, for (a) a five-element collinear array, and (b) an eight-element collinear array with $\Delta = \lambda_0$. Dotted lines delimit the range of validity of the present theory ($\rho > \lambda_0$).
- Fig. 6 Comparison between the computed azimuth pattern of the five-element, vertically polarized sector antenna described in Fig. 4a and the corresponding Gaussian fit (Eq. (E4) with $\bar{\phi}_{3dB} = 37^\circ$).
- Fig. 7 Fluctuating behavior along broadside of the peak-to-average and mid-plane-to-average power density ratios, for (a) the vertically polarized, and (b) the horizontally polarized sector arrays described in Fig. 4. Dotted lines delimit the range of validity ($\rho > \lambda_0$) of the present theory.
- Fig. 8 Prediction error along broadside for the (a) five, and (b) eight-element collinear arrays. The black curve is obtained using Eq. (13), while the gray one is obtained using Eq. (12).

- Fig. 9 Prediction error along broadside for the (a) vertically polarized and (b) horizontally polarized sector arrays described in Fig. 4. The black curve is obtained using Eq. (15); the gray one is obtained using Eq. (E8).
- Fig. 10 Prediction error along the directions (a) $\phi = 30^\circ$, and (b) $\phi = 60^\circ$ for the vertically polarized sector array described in Fig. 4a. The black curve is obtained using Eq. (15), while the gray one is obtained using Eq. (E8).
- Fig. 11 Comparison between predicted and actual compliance distance with respect to peak and average power density limits, for the (a) five, and (b) eight-element collinear arrays. The dotted lines are obtained by means of the prediction formulae (16), whereas the solid lines are derived from the field values computed using NEC. The corresponding prediction error is reported in the encapsulated graph.
- Fig. 12 Comparison between predicted and actual compliance distance with respect to peak and average power density limits, for the (a) vertically polarized, and (b) horizontally polarized sector arrays described in Fig. 4. The dotted lines are obtained by means of the prediction formulae (16), whereas the solid lines are derived from the field values computed using NEC. The corresponding prediction error is reported in the encapsulated graph.
- Fig. 13 Reference frame defined by the array beam down-tilt angle γ .
- Fig. 14 Comparison between predicted and actual compliance distance with respect to peak and average power density limits, for the eight-element collinear array exhibiting $\gamma = 9.5^\circ$ beam down-tilt. The dotted lines are obtained by means of the prediction formulae (F4), whereas the solid lines are derived from the field values computed using NEC. The corresponding prediction error is reported in the encapsulated graph.

TABLE I: Definition of the parameters in Eqs. (16). Depending on the exposure standard, the applicable limit S is either \bar{S} or \hat{S} .		
ARRAY TYPE	ρ_0	q
OMNIDIRECTIONAL	$D_A \frac{L}{2}$	$\frac{W_{rad}}{\pi L^2 D_A S}$
SECTOR	$\frac{\bar{\phi}_{3dB}}{6} D_A L$	$\frac{3W_{rad} 2^{-\left(\frac{\phi}{\bar{\phi}_{3dB}}\right)^2}}{\bar{\phi}_{3dB}^2 L^2 D_A S}$

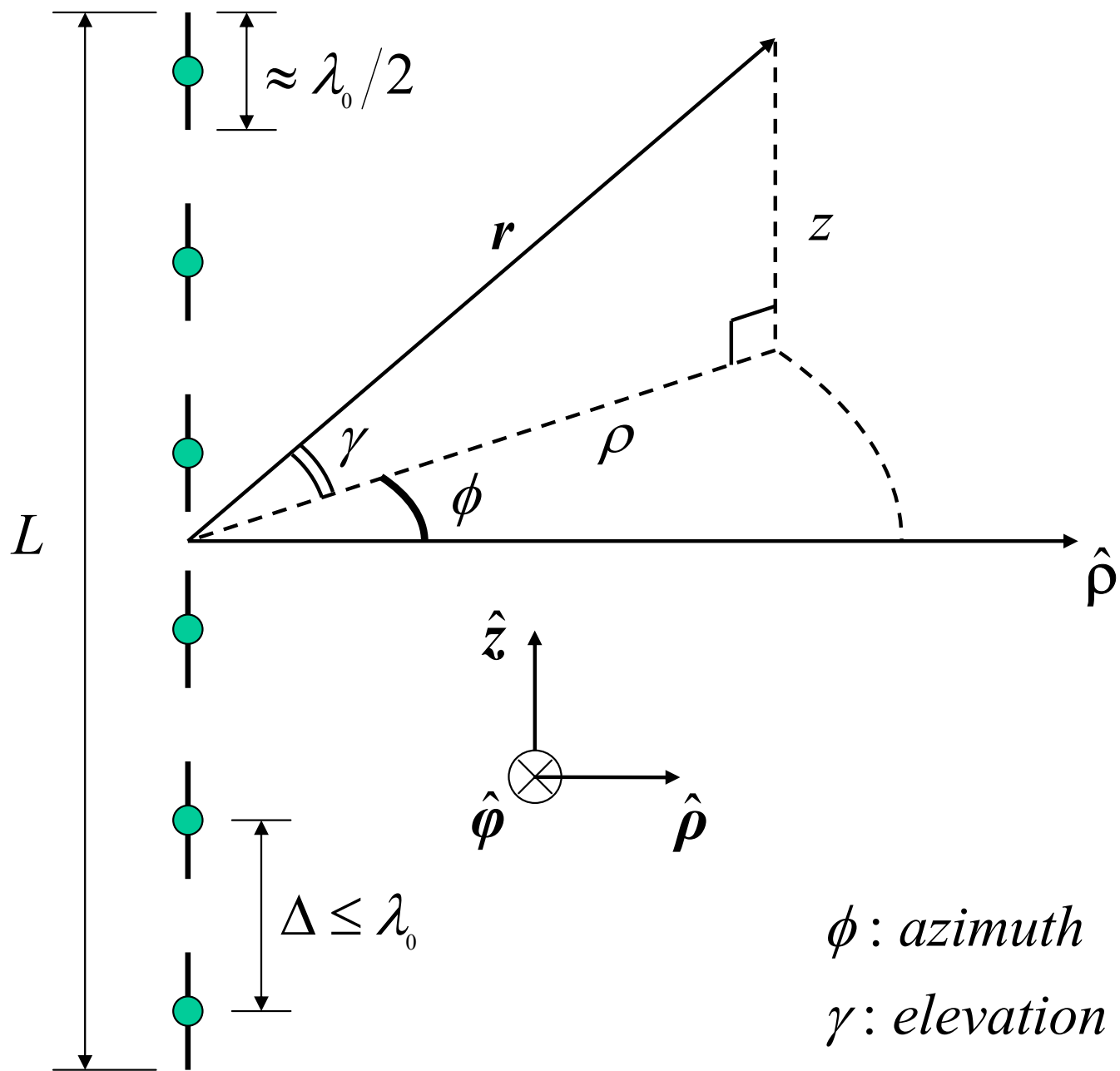


FIG. 1

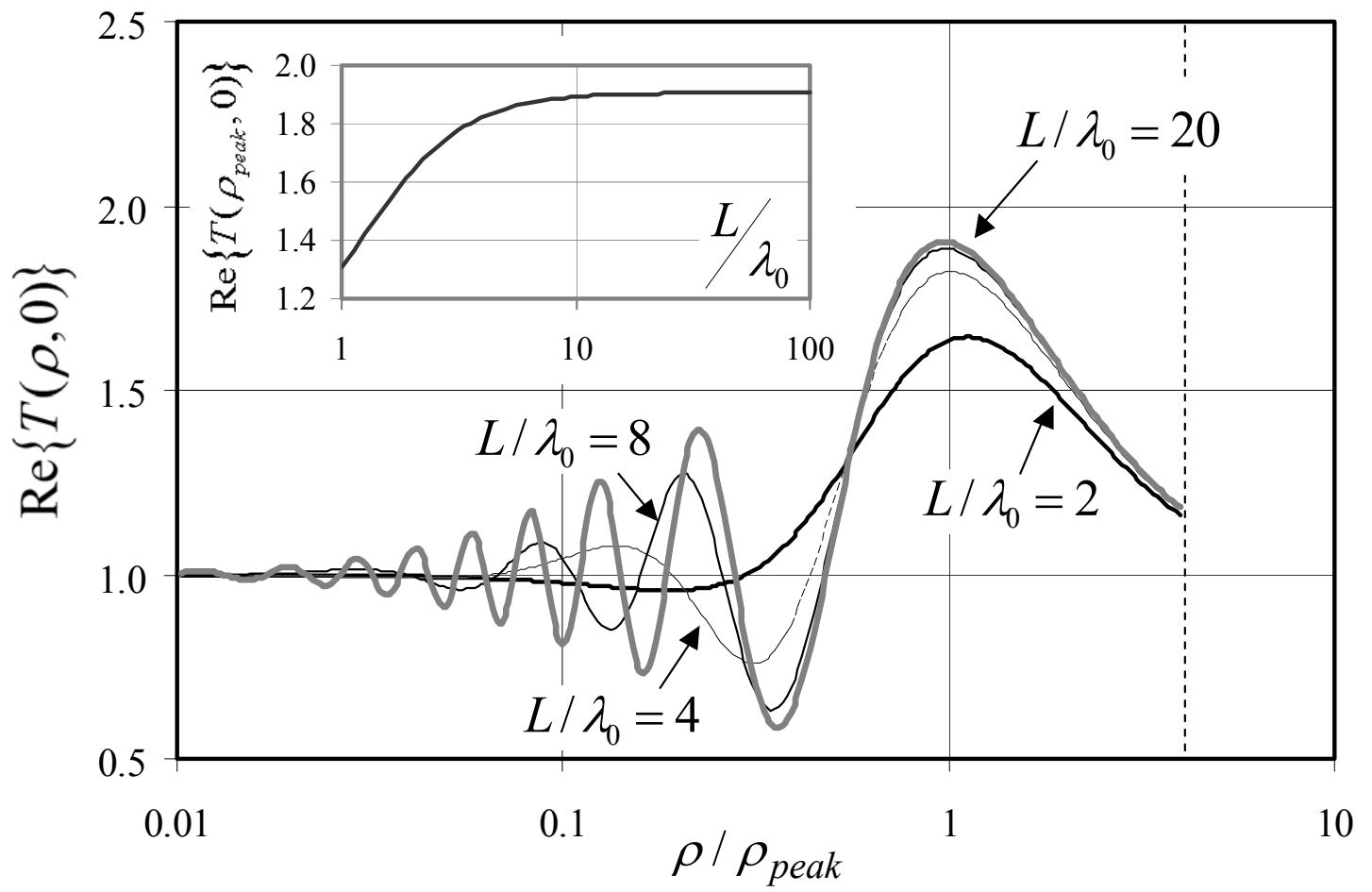


FIG. 2

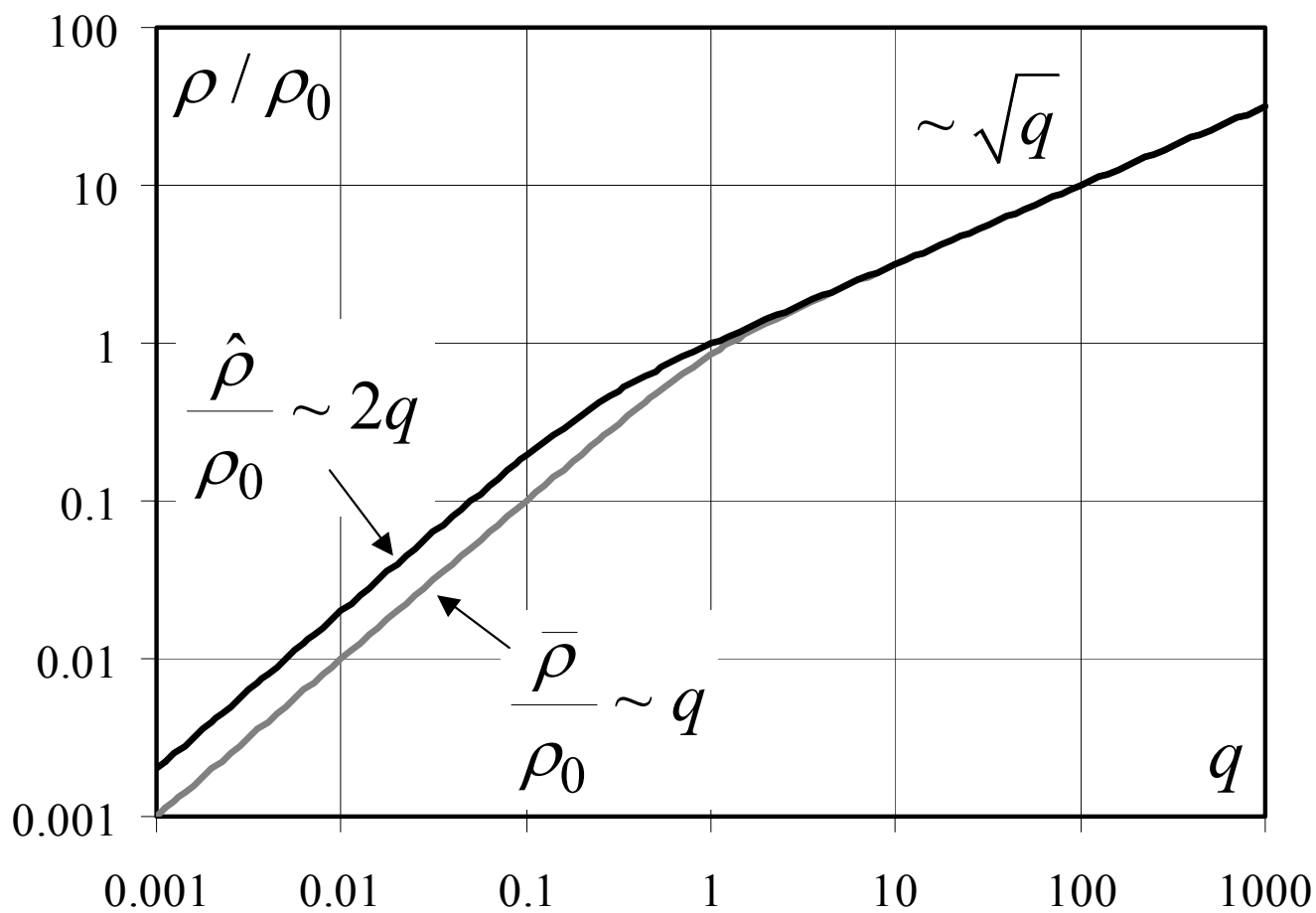


FIG. 3a

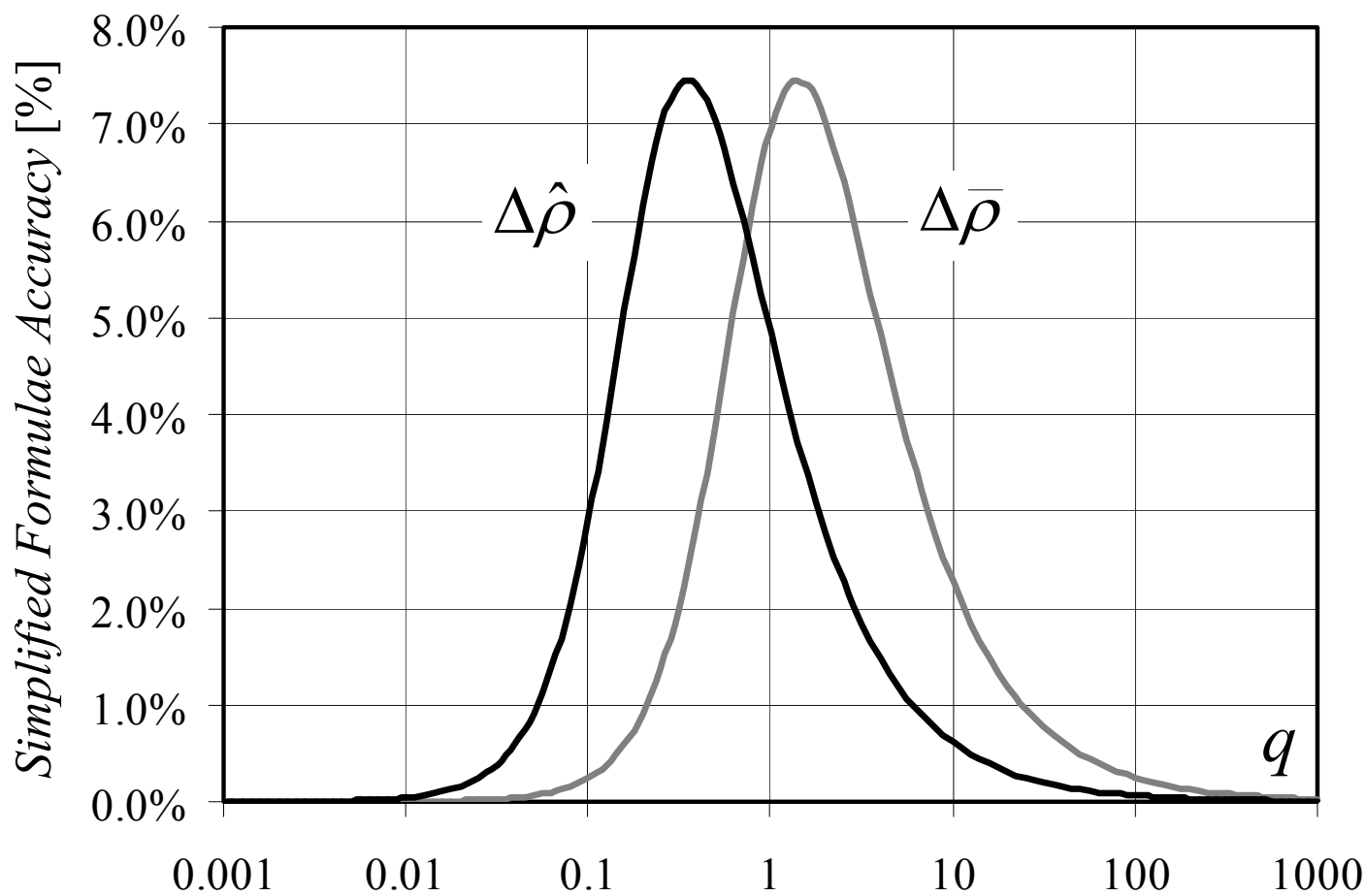


FIG. 3b

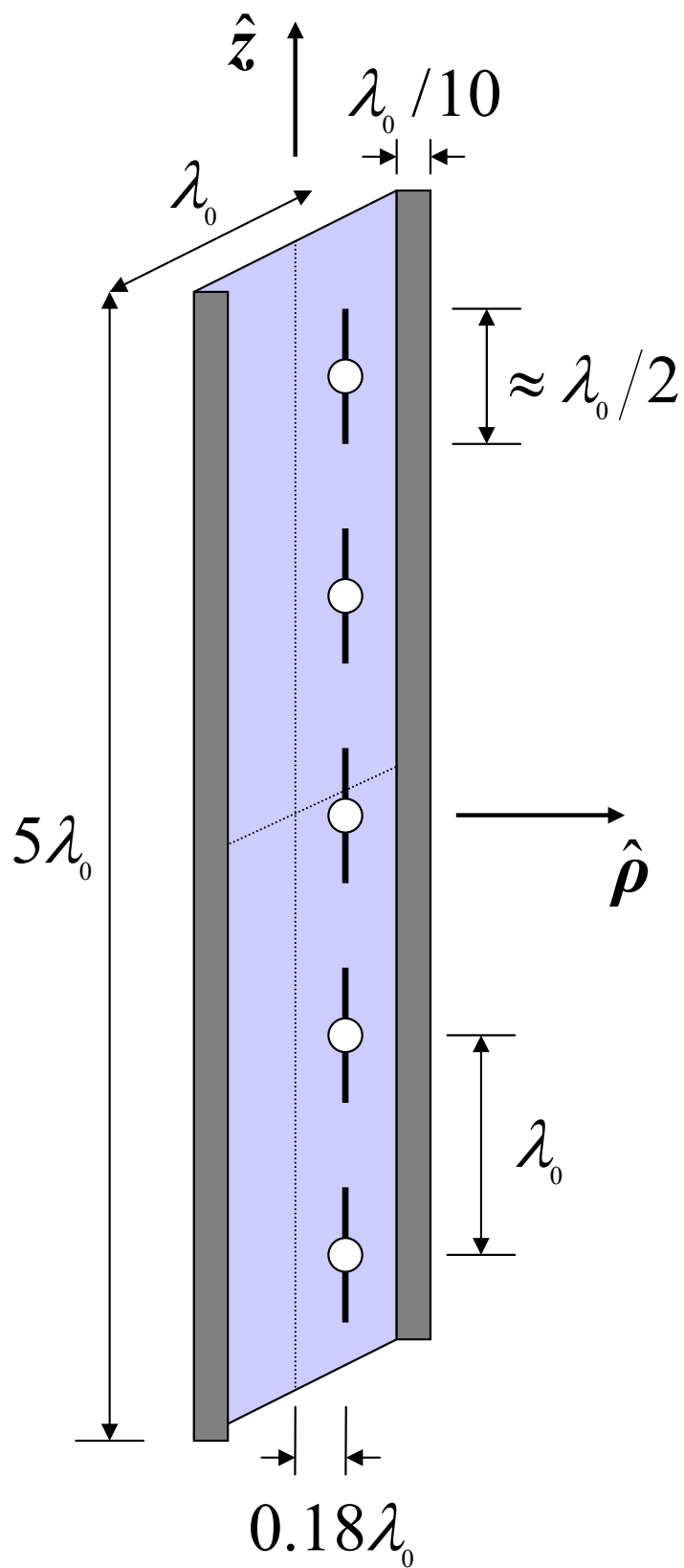


FIG. 4a

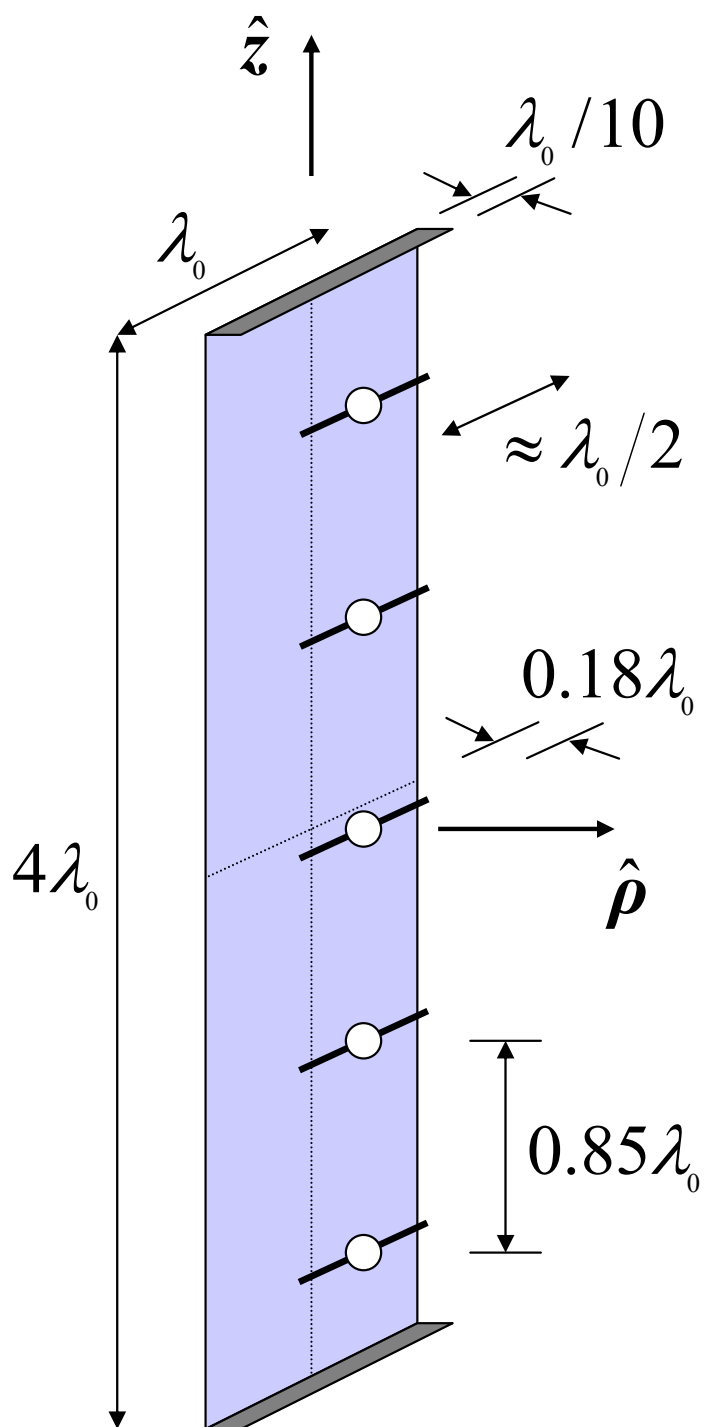


FIG. 4b

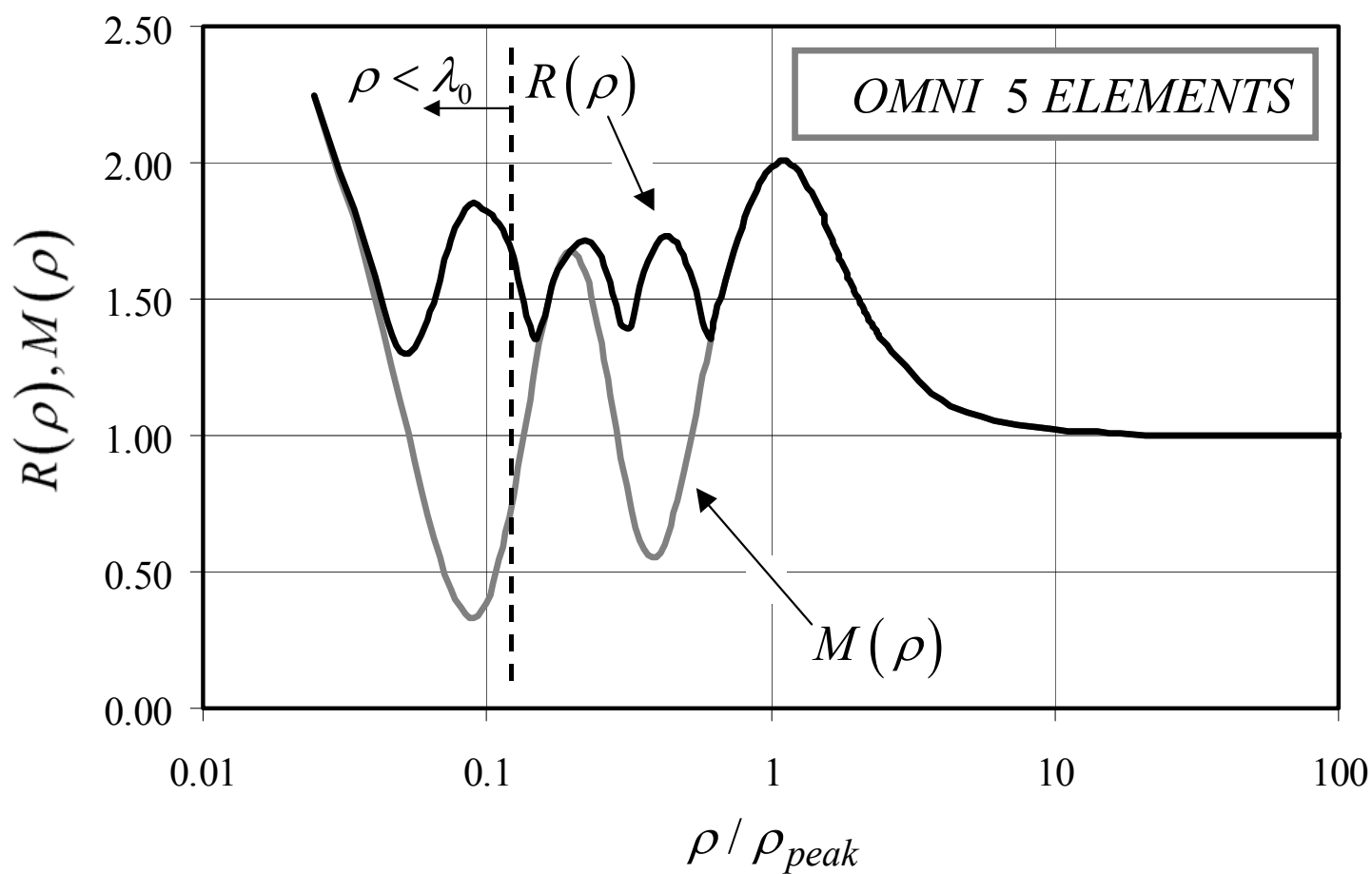


FIG. 5a

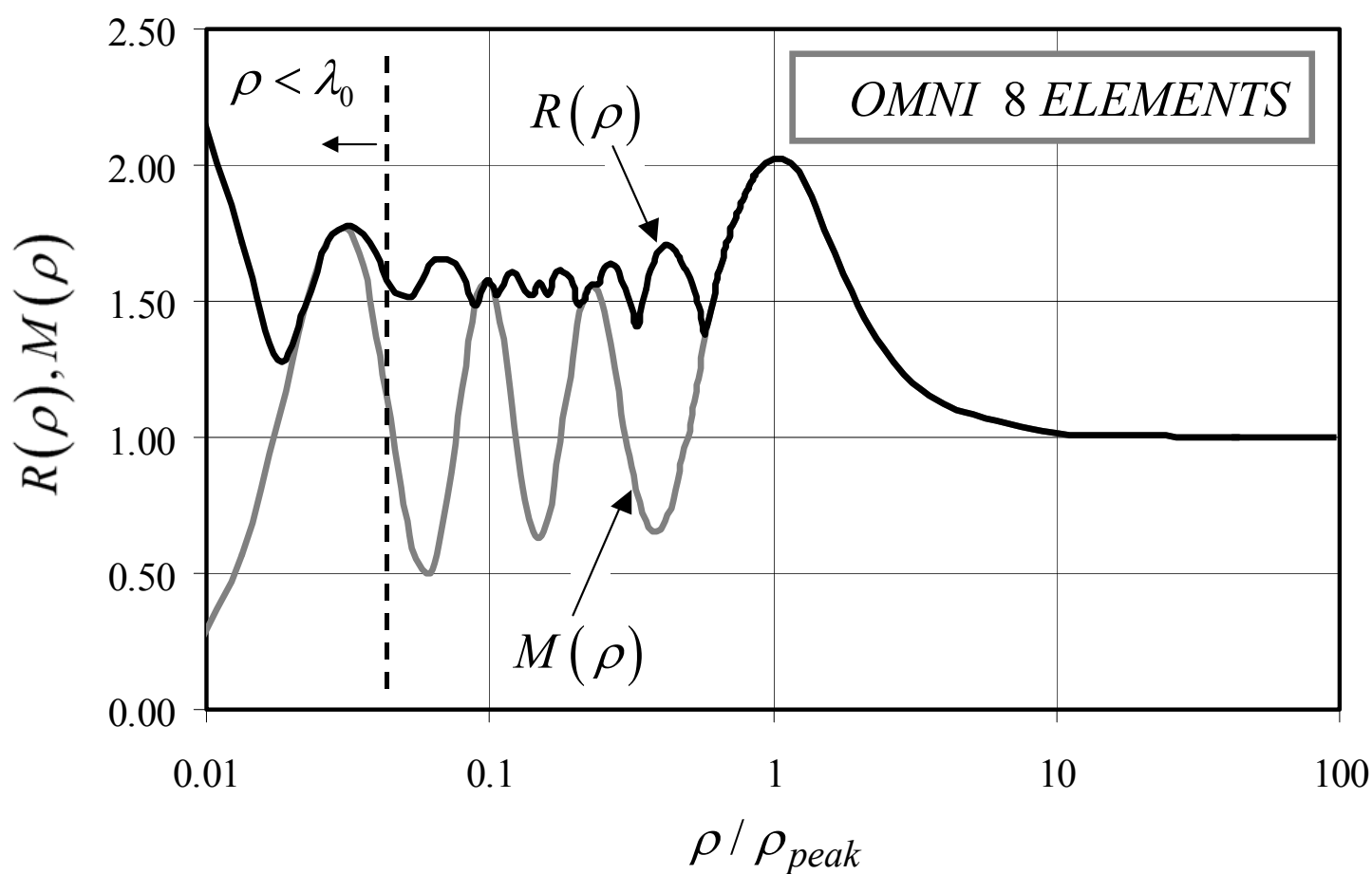


FIG. 5b

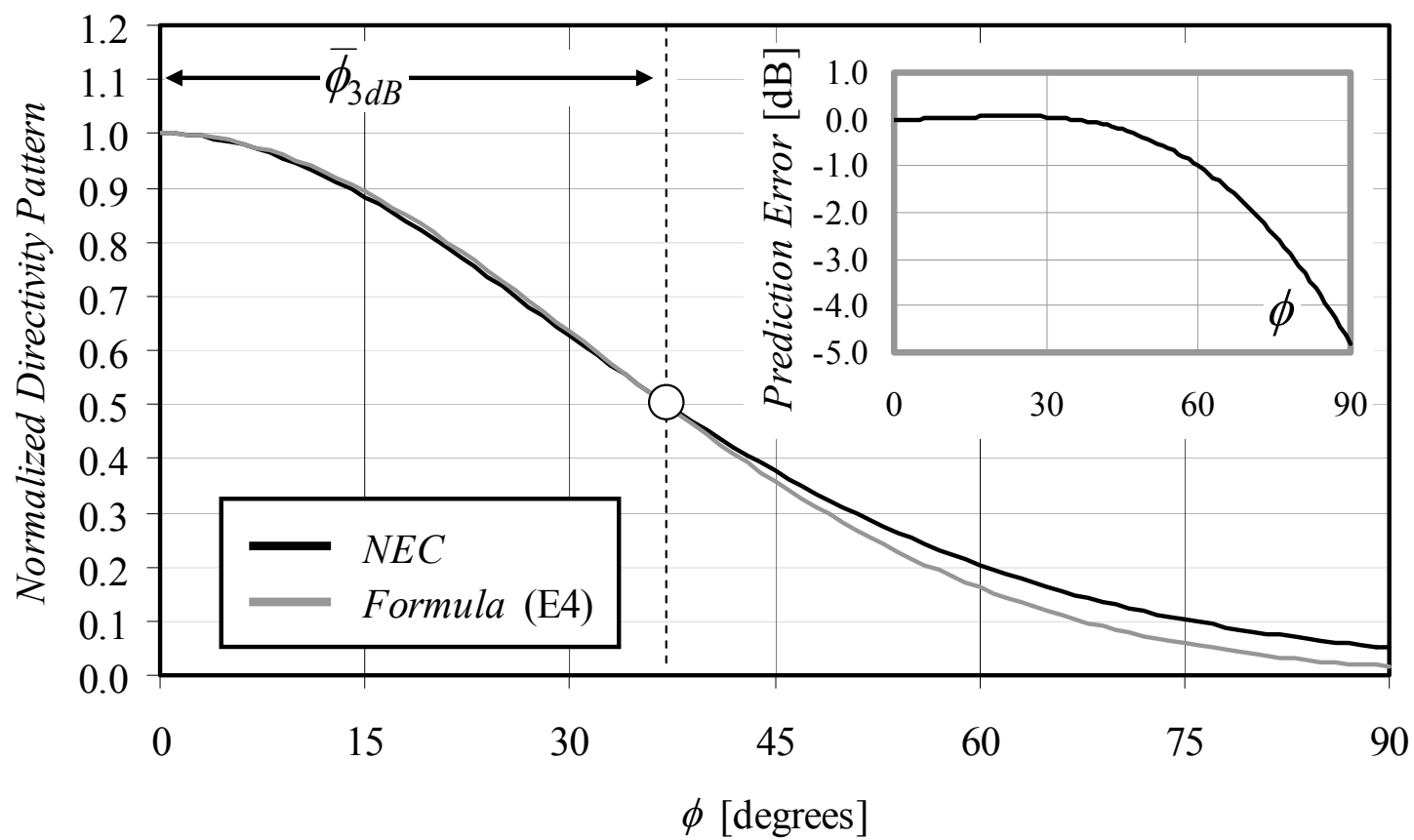


FIG. 6

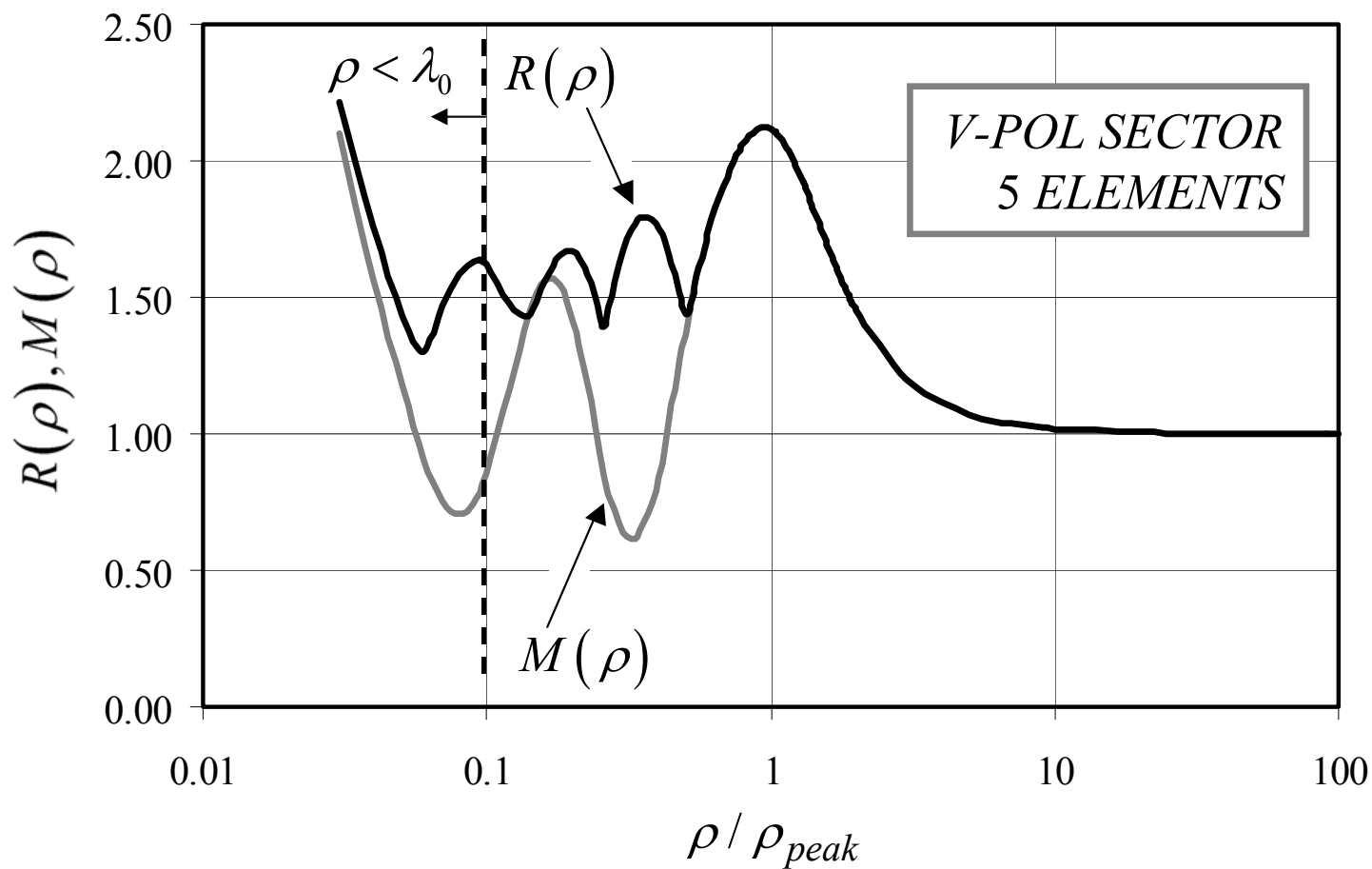


FIG. 7a

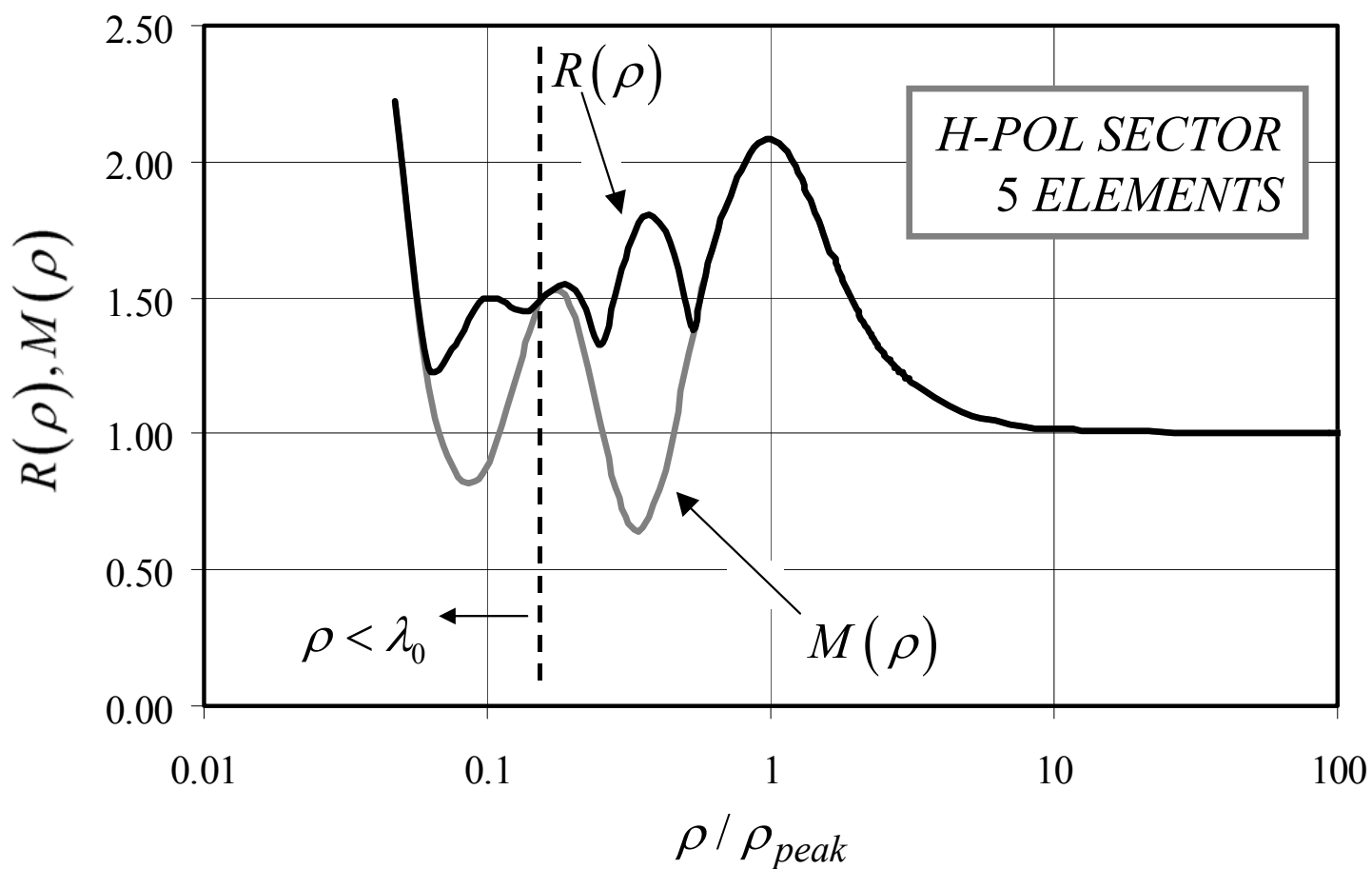


FIG. 7b

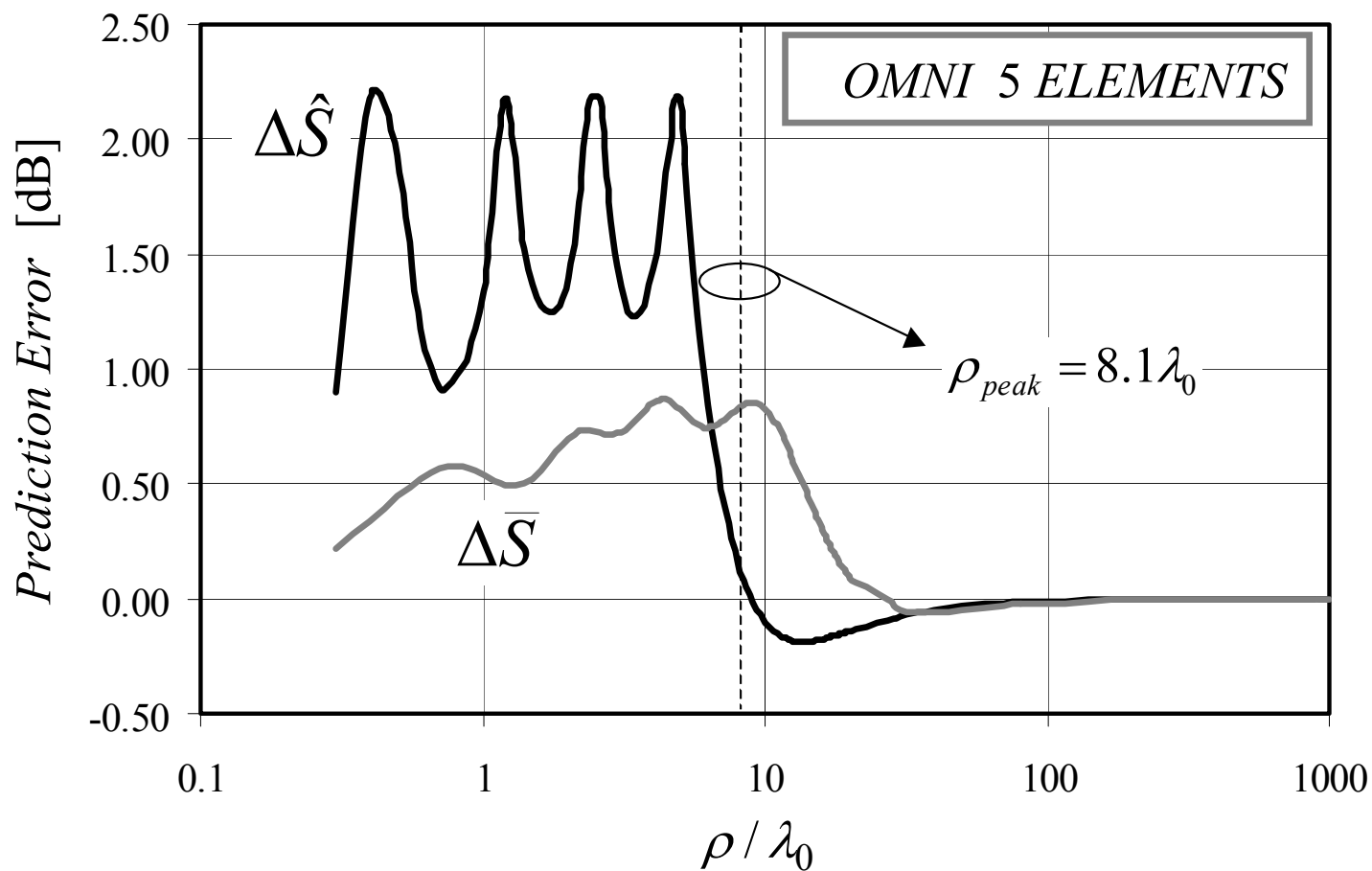


FIG. 8a

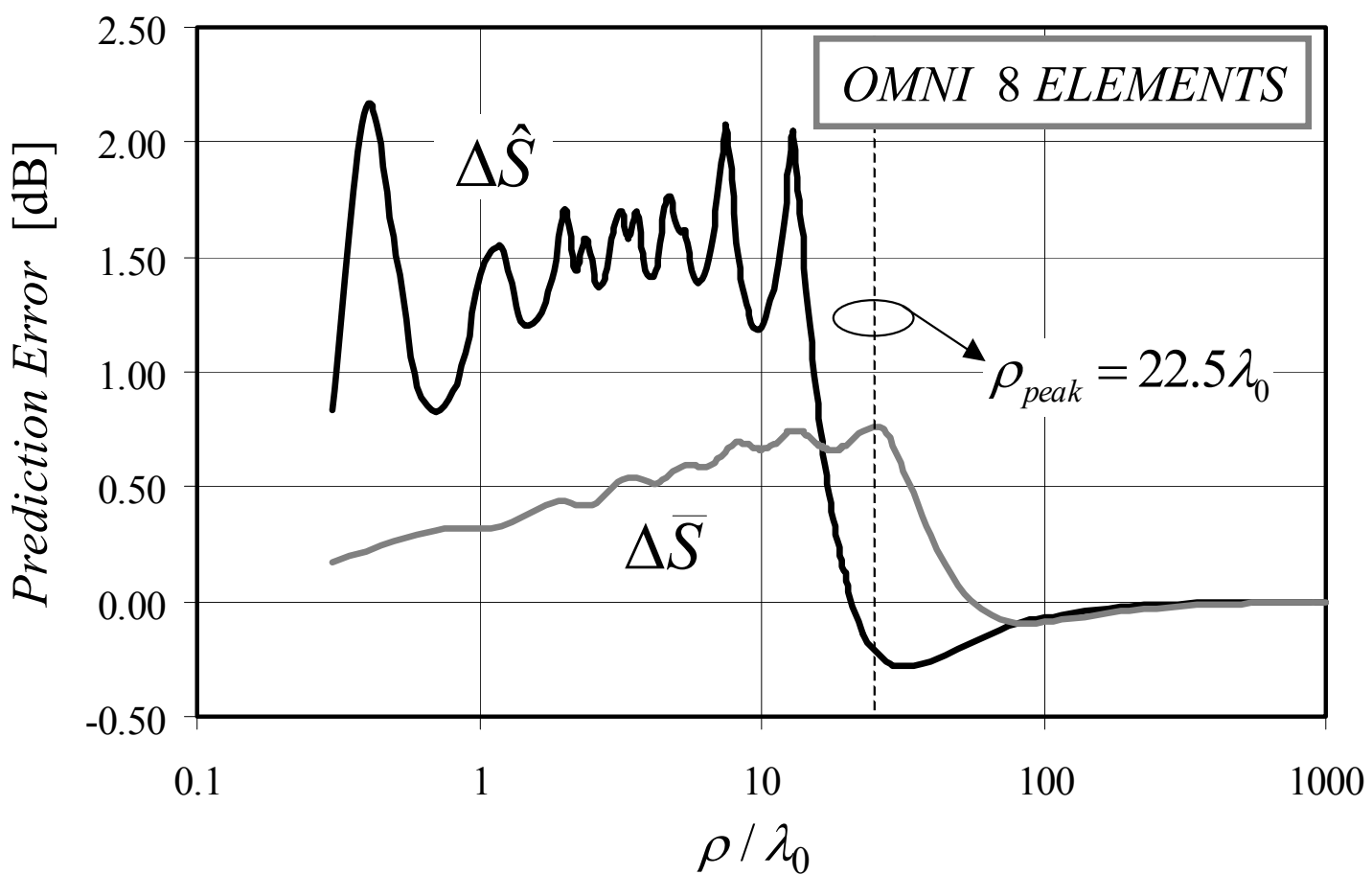


FIG. 8b

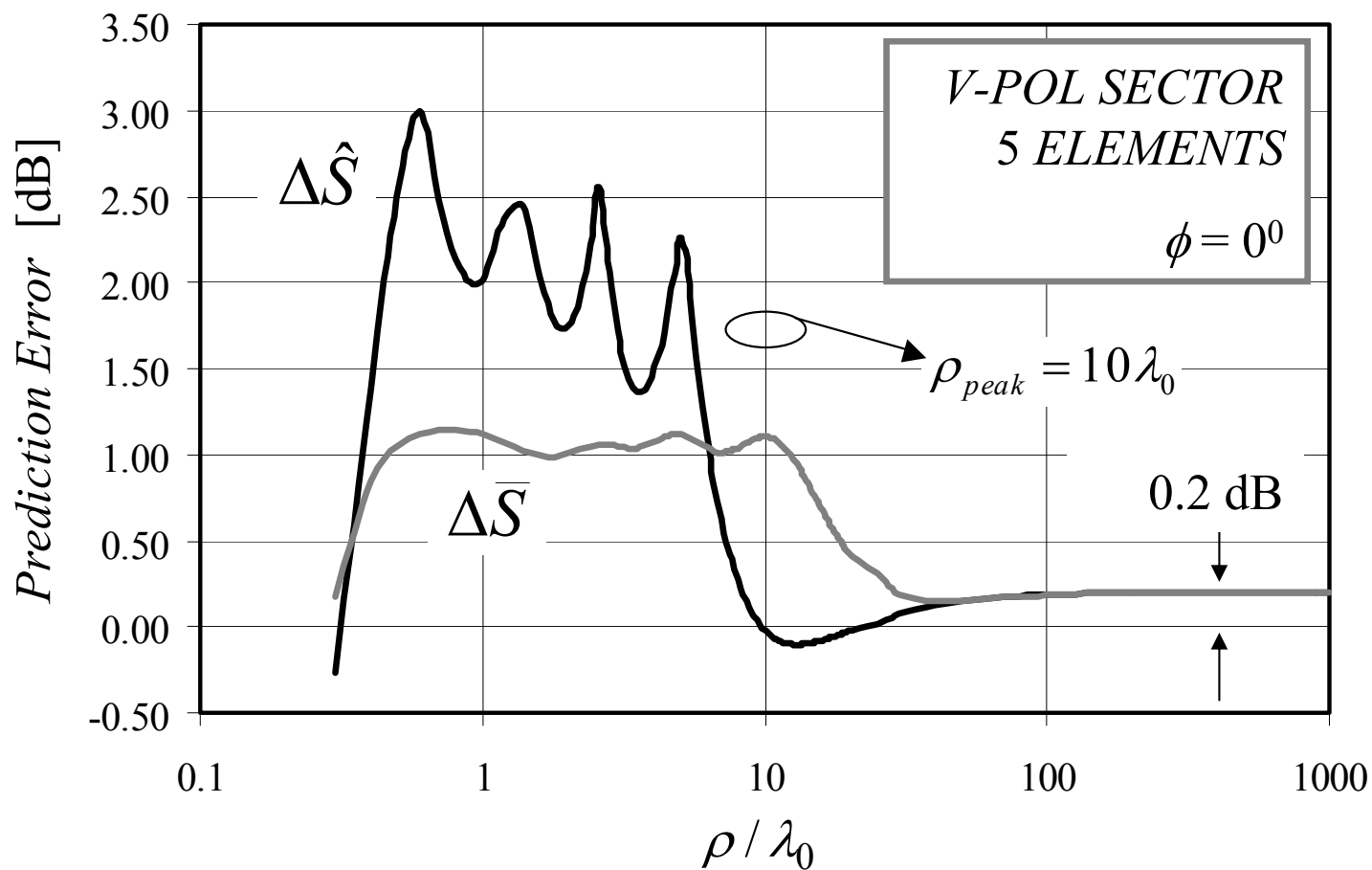


FIG. 9a

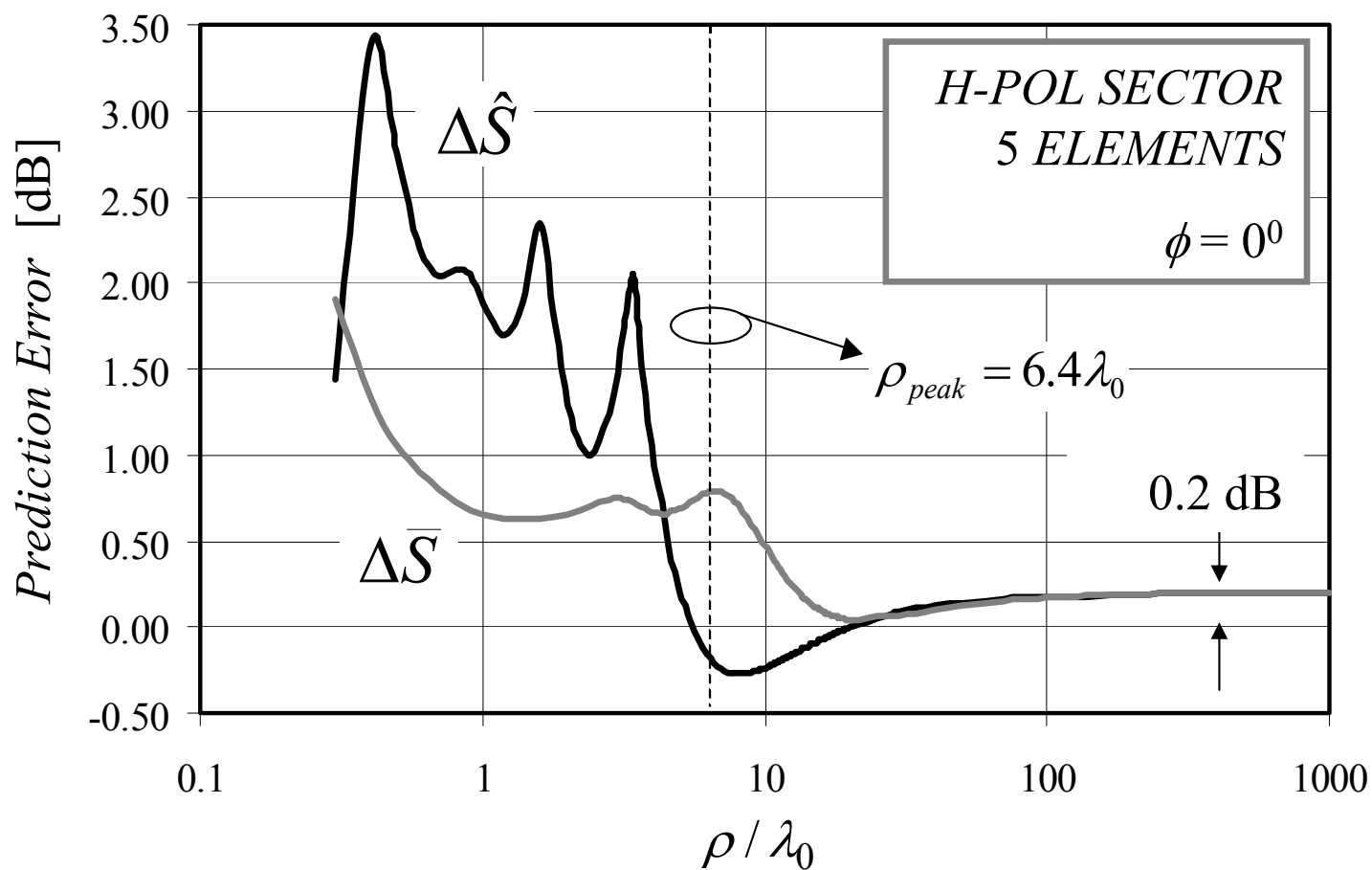


FIG. 9b

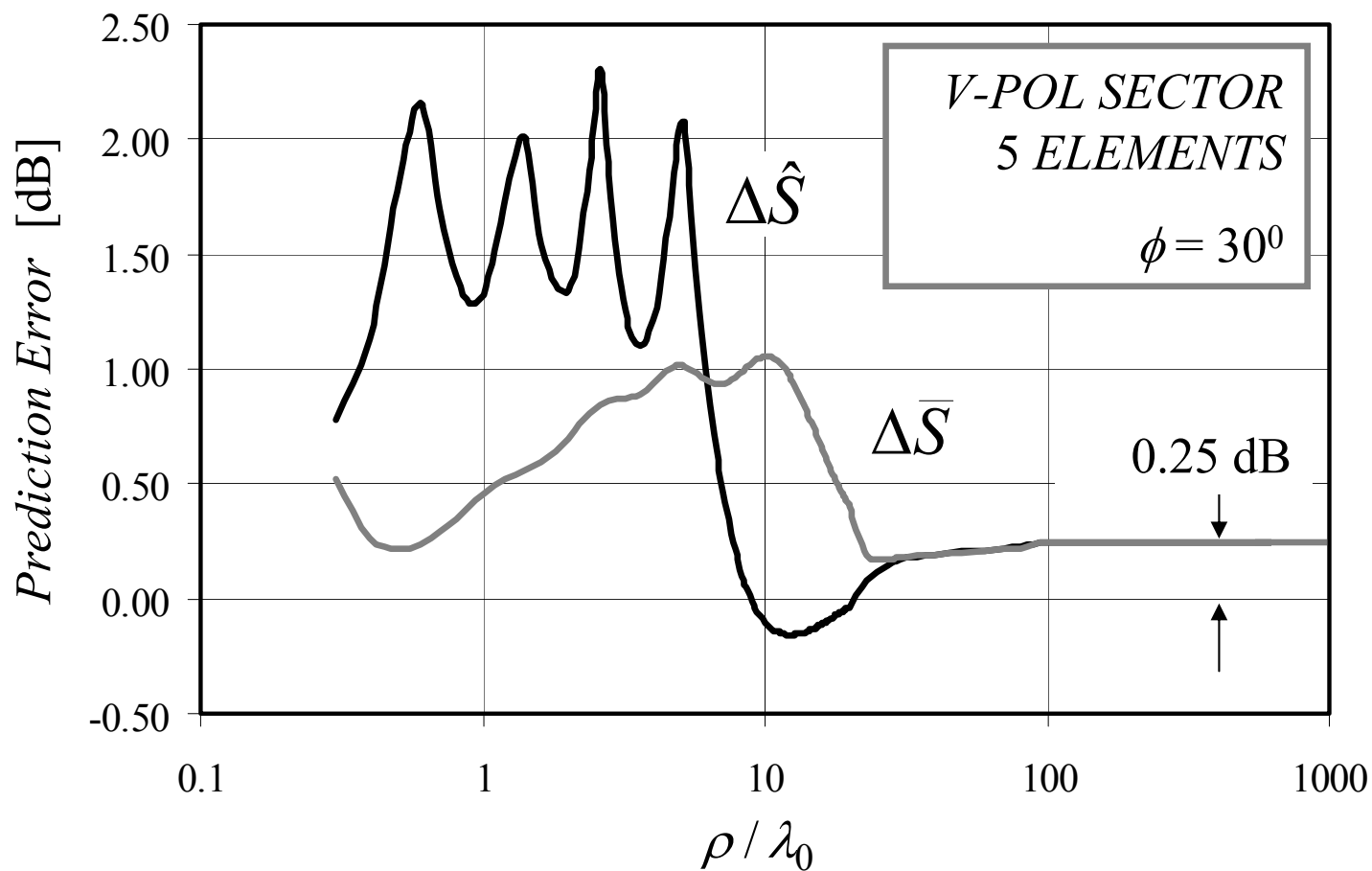


FIG. 10a

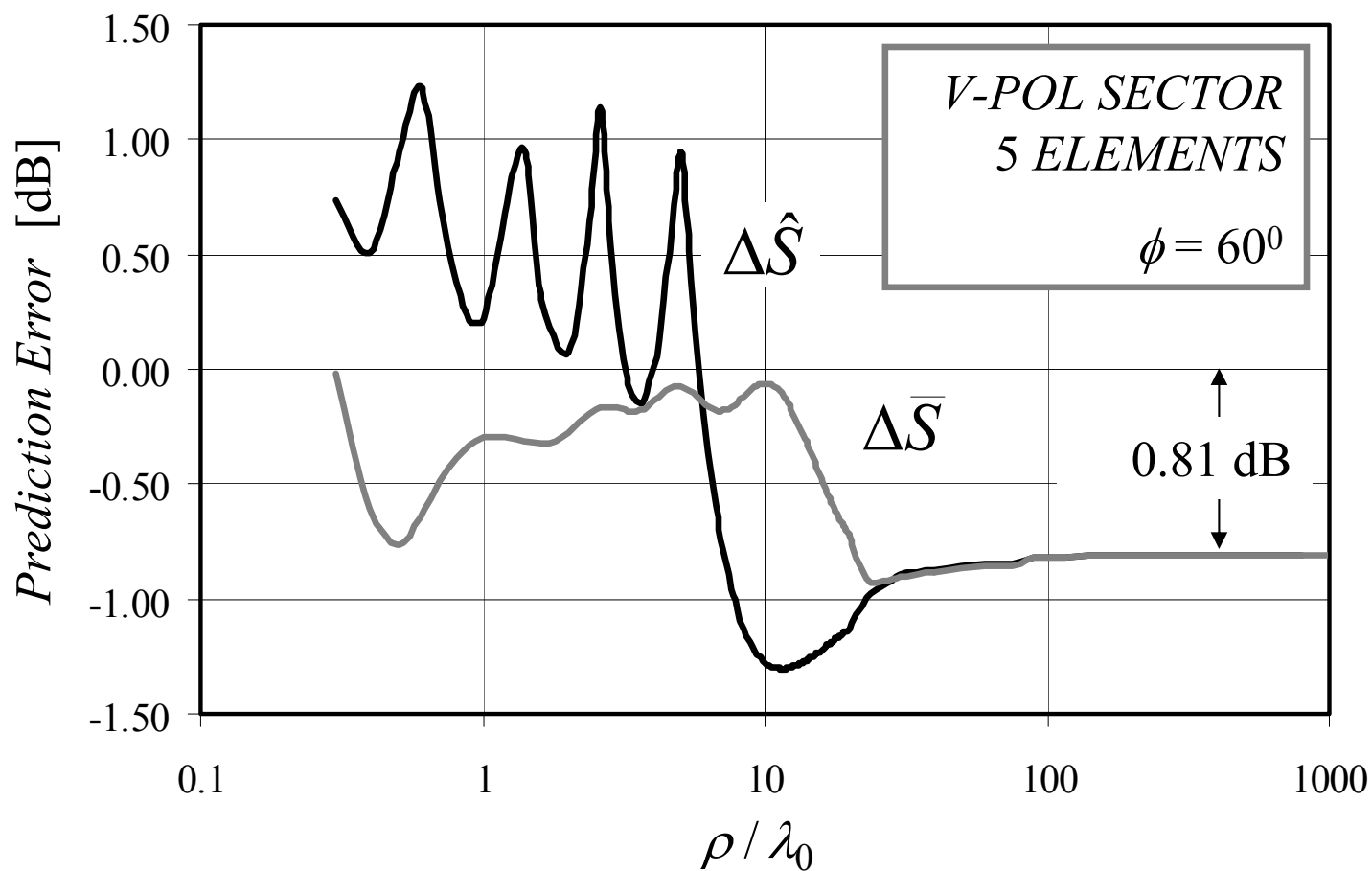


FIG. 10b

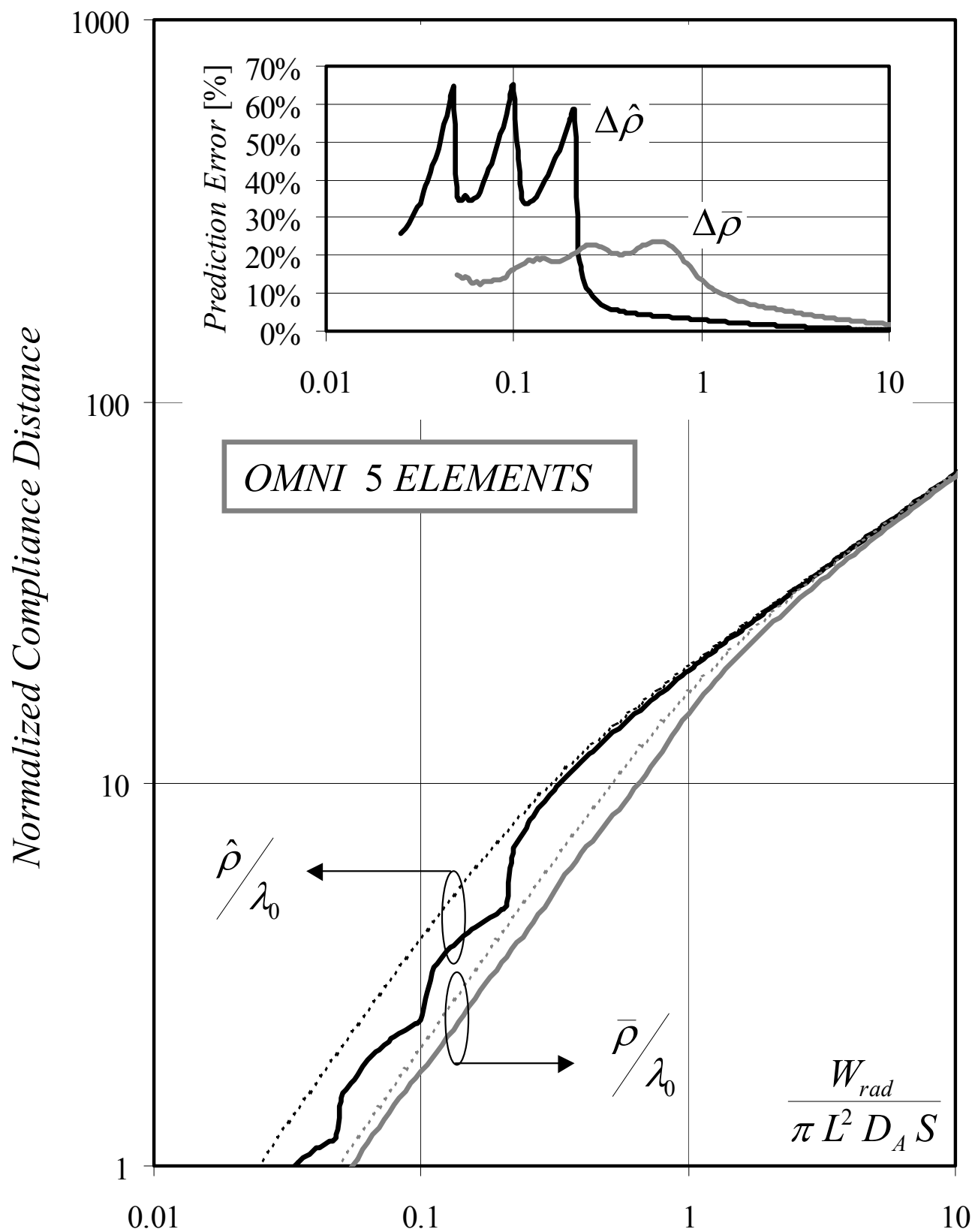


FIG. 11a

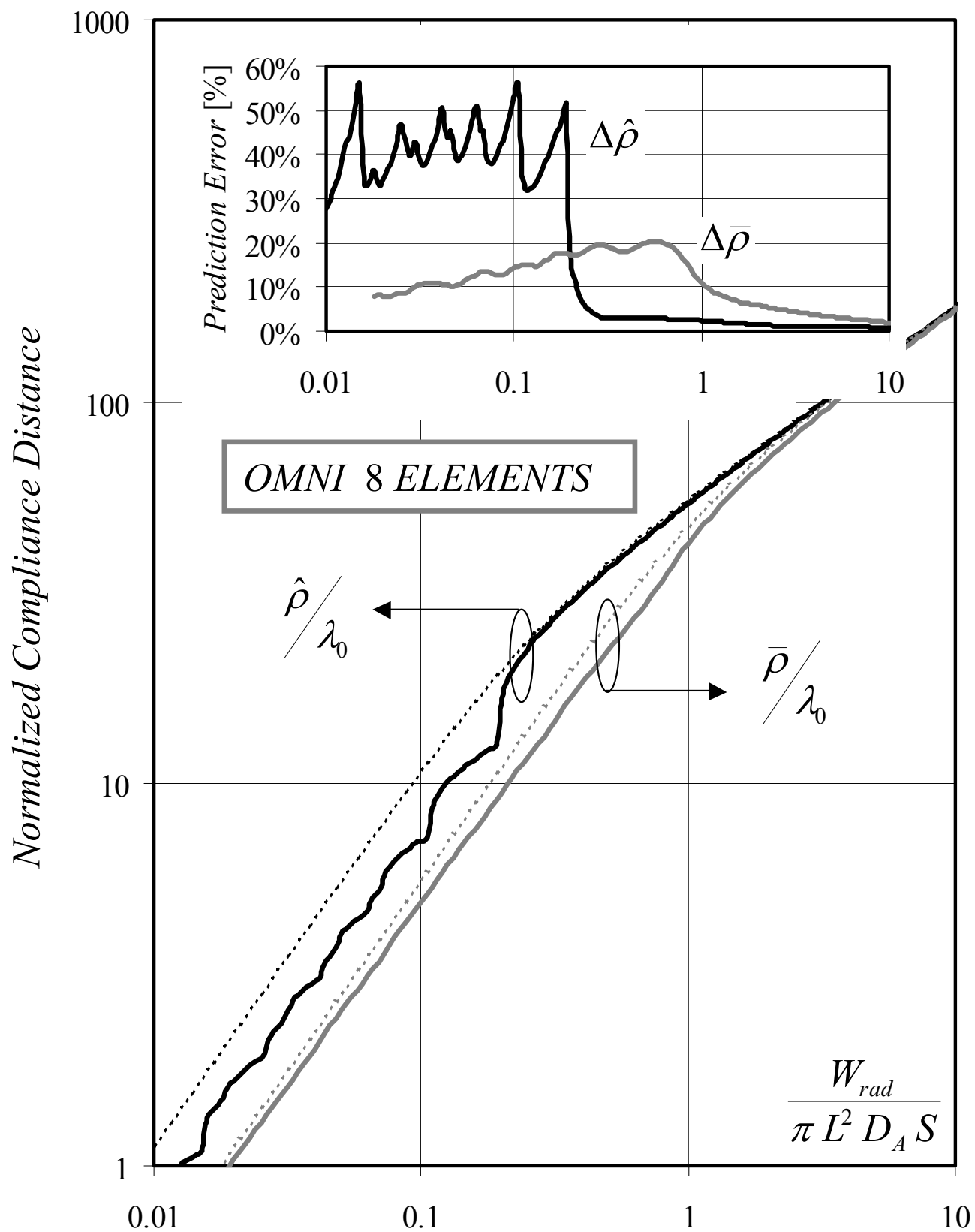


FIG. 11b

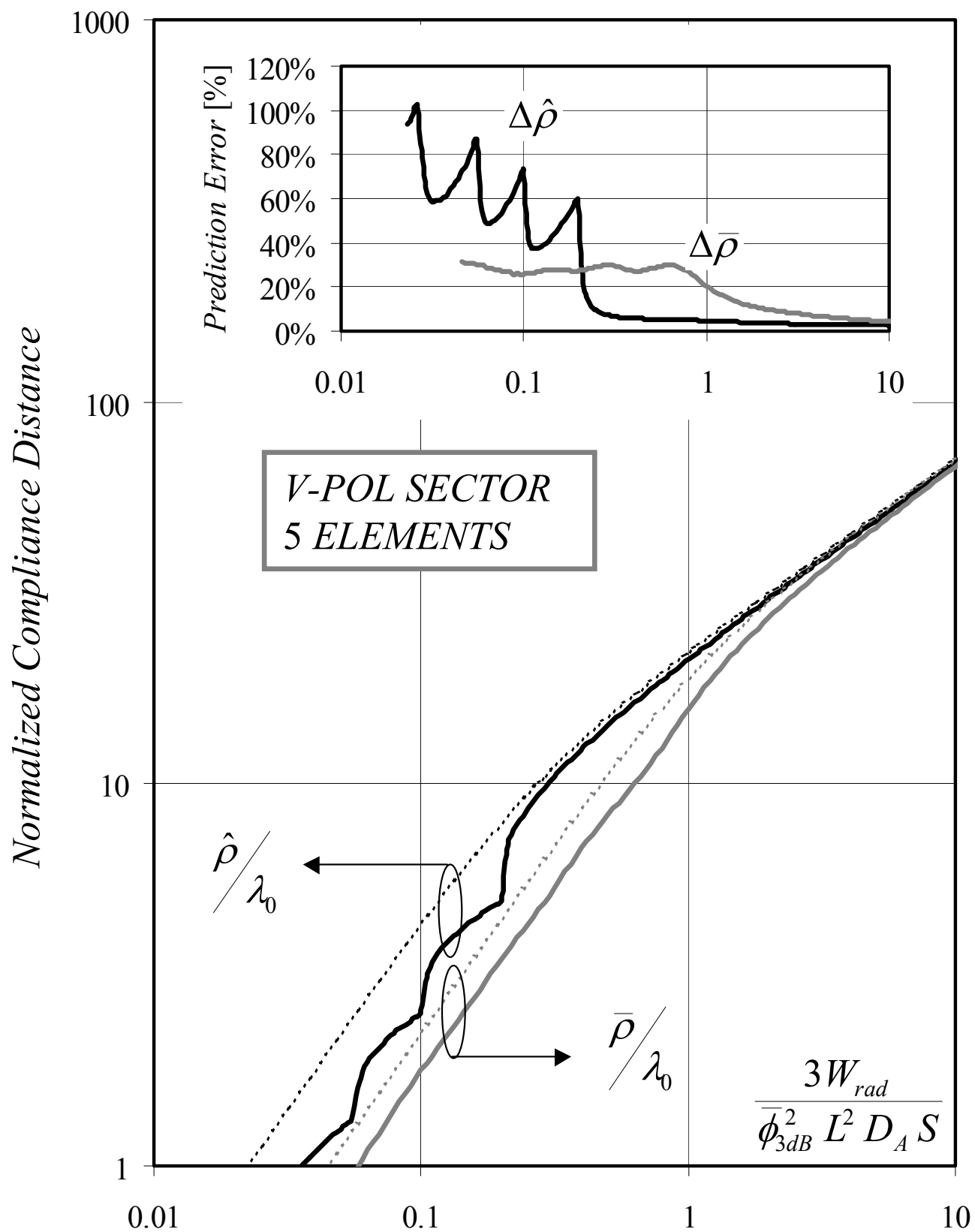


FIG. 12a

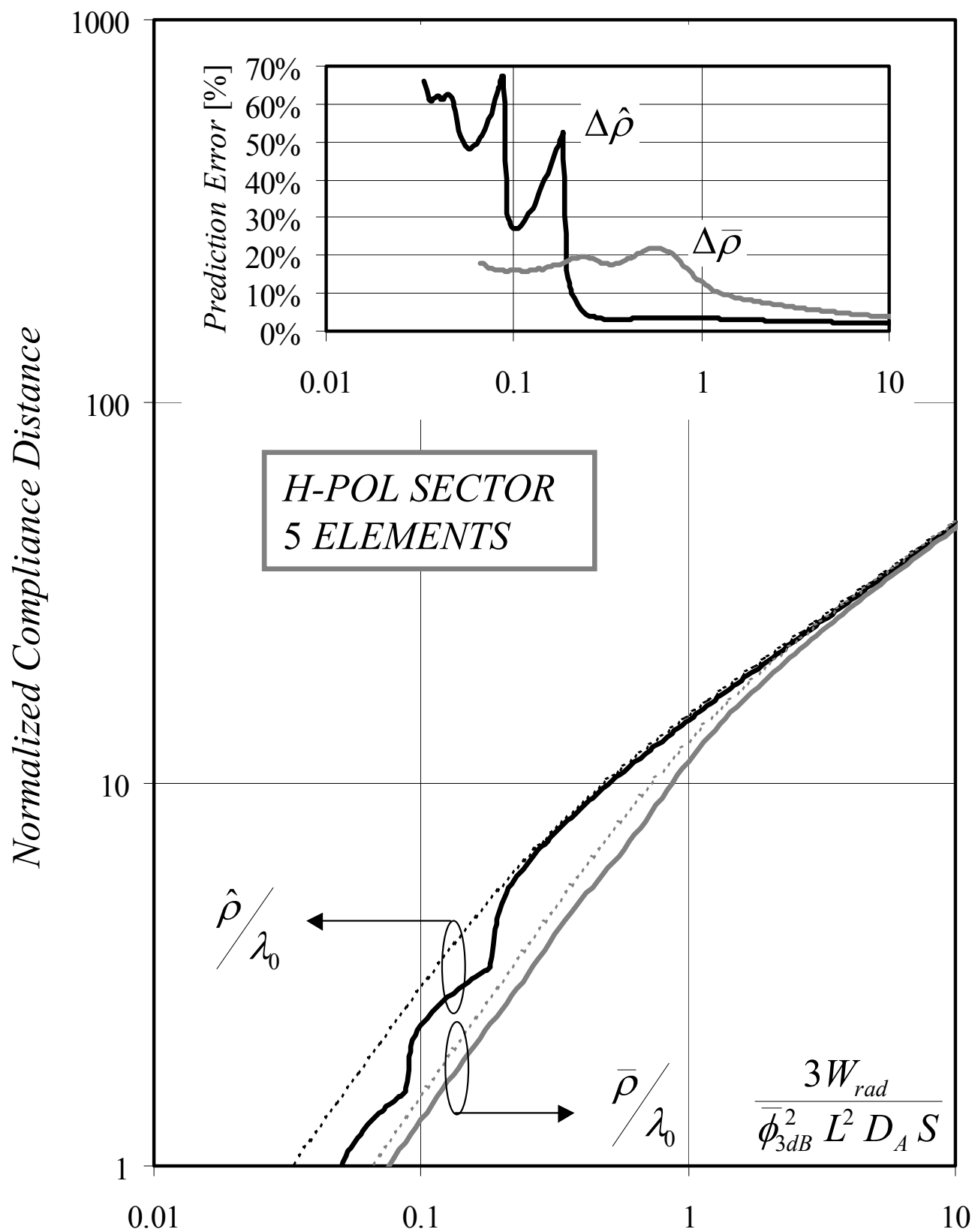


FIG. 12b

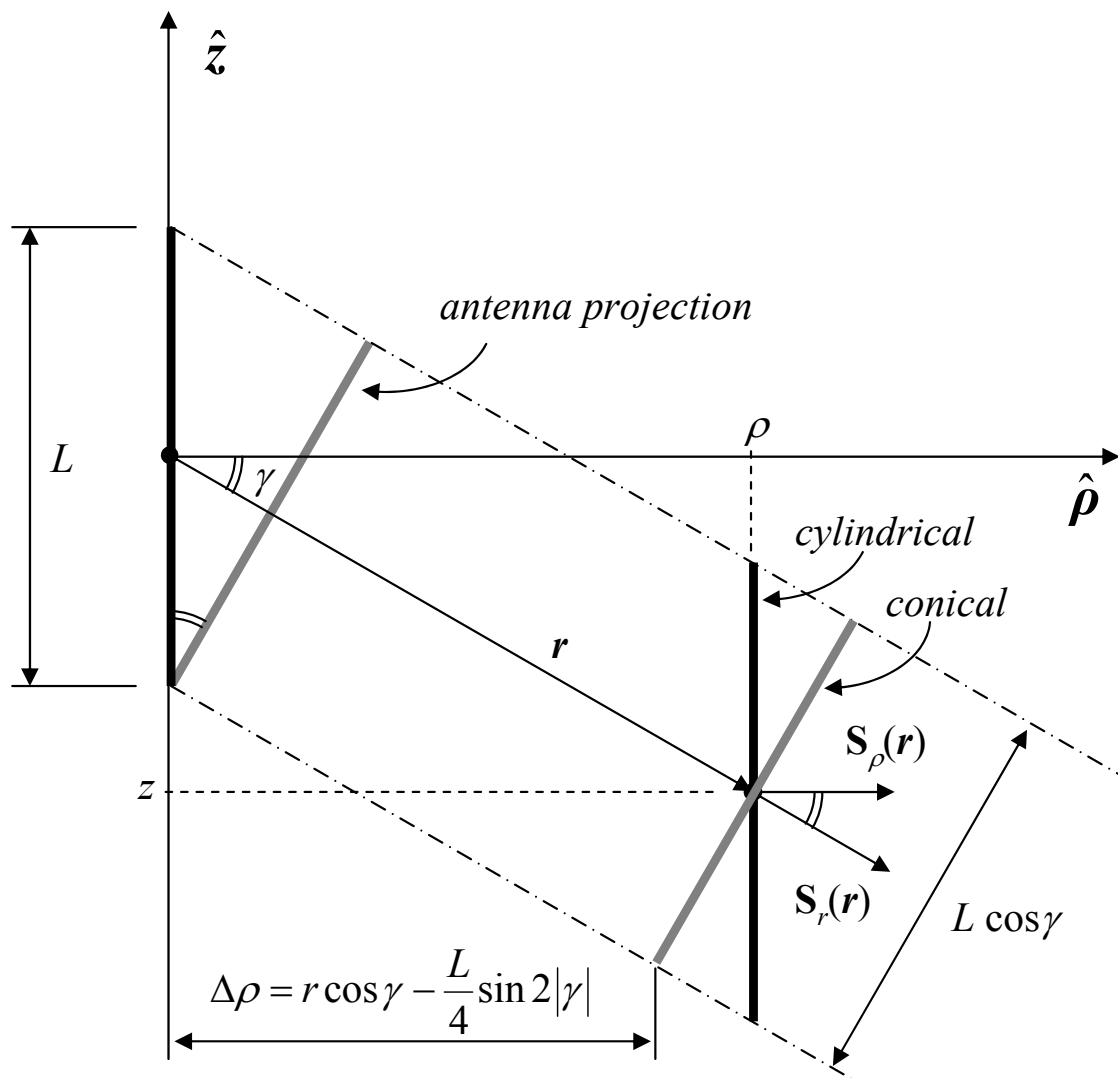


FIG. 13

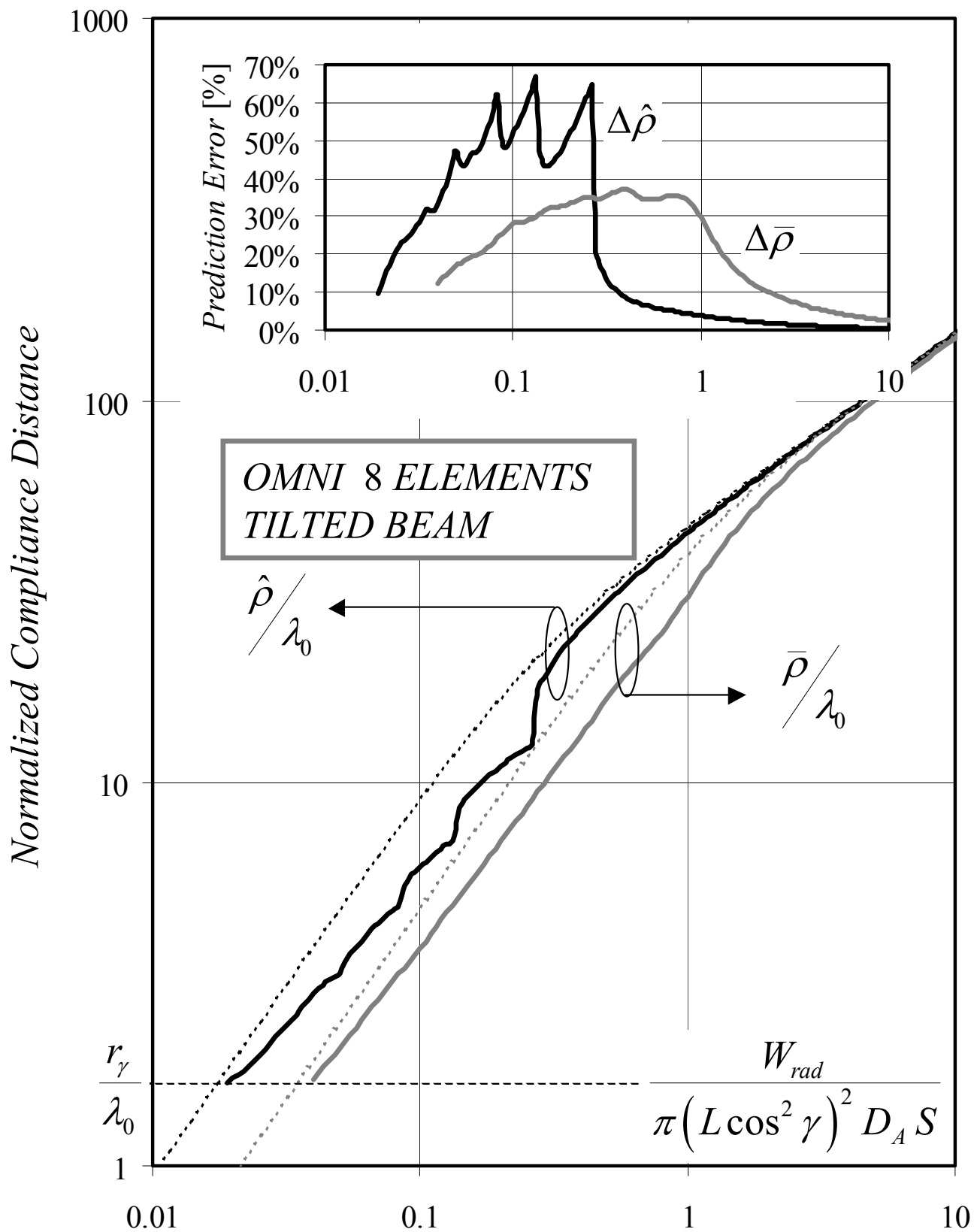


FIG. 14